Check for updates

ELECTROCHEMISTRY

Redesigning protonic ceramic electrochemical cells to lower the operating temperature

Fan Liu[1], David Diercks[2], Praveen Kumar[2], Arim Seong[3], Mohammed Hussain Abdul Jabbar[4], Cenk Gumeci[4], Yoshihisa Furuya[4], Nilesh Dale[4], Takanori Oku[5], Masahiro Usuda[5], Pejman Kazempoor[6], Iman Ghamarian[6], Lin Liu[7], Liyang Fang[1], Di Chen[1], Zixian Wang[1], Stephen Skinner[3], Chuancheng Duan[1,8]*

Copyright © 2025 The Authors, some rights reserved; exclusive licensee American Association for the Advancement of Science. No claim to original U.S. Government Works. Distributed under a Creative Commons Attribution NonCommercial License 4.0 (CC BY-NC).

Protonic ceramic electrochemical cells (PCECs) can operate at intermediate temperatures (450° to 600°C) for power generation and hydrogen production. However, the operating temperature is still too high to revolutionize ceramic electrochemical cell technology. Lowering the operating temperature to <450°C will enable a wider material choice and reduce system costs. We present approaches to redesigning PCECs via readily fabricated single-grain–thick, chemically homogeneous, and robust electrolytes and a nano-micro positive electrode. At 450°C, the PCECs achieve a peak power density of 1.6 watt per square centimeter on H_2 fuel, 0.5 watt per square centimeter on NH_3 fuel, and 0.3 watt per square centimeter on CH_4 fuel in fuel cell mode. In steam electrolysis mode, a current density of >0.6 ampere per square centimeter with a Faradaic efficiency of >90% is achievable at 1.4 volt and 400°C. In addition, exceptional durability (>2000 hours) has been demonstrated, with a degradation rate of <0.01 millivolt per 100 hours in fuel cell mode at 400°C.

INTRODUCTION

Ceramic electrochemical cells are uniquely capable of generating power using a wide range of fuels, including hydrogen, hydrocarbons, and ammonia, and producing green hydrogen (H_2) via steam electrolysis, with higher energy efficiencies than low-temperature water electrolysis technologies (*1*–*8*). The main issue of ceramic electrochemical cells for scaled energy conversion originates from the high operating temperature, which leads to limited material choices for interconnects and sealants, expensive balance of plants (BOPs), slow start-up and shutdown cycles, and high degradation rates, inevitably limiting their scale-up and commercialization (*9*). Lowering the temperature to 300° to 450°C can transform the architecture and operation of ceramic electrochemical cells (Fig. 1). For example, when the temperature is reduced to even below 350°C, inexpensive stainless steel interconnects, polymeric sealants, and ready-made BOPs can be used, while the thermal cycling stability, system reliability, and applicability in the portable power and transportation markets and distributed chemical manufacturing industries can be enhanced (*10*). In addition, lower operating temperatures in steam electrolysis mode enable integration with a broader range of waste heat sources, which can reduce the electrical energy consumption required for hydrogen production.

There has been great progress in lowering the operating temperature of ceramic electrochemical cells. Fabrication of ultrathin electrolytes and engineering of the electrodes enable lowering of the oxygen-ion solid oxide electrochemical cell (O-SOEC) operating temperature to 500°C (*11*). However, because of the high activation energy of oxygen-ion conduction, the performance of O-SOECs is poor at <500°C. Therefore, over the past decade, protonic ceramic electrochemical cells (PCECs) have been revived, aiming to efficiently generate power and produce clean H_2 at <500°C. The most recent report on the acid etching process presented successful reduction of the contact resistance between the electrolyte and positive electrode to enhance the PCEC performance at 450° to 600°C (*12*), with a fuel cell peak power density of 0.65 W cm^{-2} demonstrated at 450°C on H_2-O_2 (Fig. 2A). Despite these remarkable achievements, the PCEC performance at <450°C is still far below the performance that can be routinely attained at 600°C.

The target is to develop ultrahigh-power low-temperature PCECs (UHP LT-PCECs) that operate at 300° to 450°C and can achieve performance comparable to that of intermediate-temperature PCECs (500° to 600°C) and O-SOECs. Duan *et al.* (*13*) predicted the target PCEC fuel cell performance according to the intrinsic conductivity of state-of-the-art proton-conducting electrolytes, suggesting that exceptional performance is feasible at 300° to 400°C and that fuel cell power densities >2.0 W cm^{-2} could be reached (fig. S1). Although advanced electrolyte fabrication approaches and extensive triple-conducting positive electrodes have been demonstrated (*11*, *14*–*19*), the predicted PCEC performance has not yet been fully realized, which is still ascribed to the high ohmic resistance and positive electrode polarization resistance. Figure S2 shows that the area-specific electrode polarization resistance (ASR_P) dominates the total resistance at <450°C. There are few PCECs that can operate at <450°C, highlighting the challenges of lowering the operating temperatures of PCECs. These results suggest that both the electrolyte and positive electrode should be redesigned to lower the PCEC operating temperature.

RESULTS

Redesigned PCECs achieving unprecedented fuel cell and steam electrolysis performance at <450°C

Here, we tailored the electrolyte-negative electrode pair and developed a nano-micro positive electrode to redesign and construct UHP LT-PCECs. First, without using complicated and expensive

[1]Department of Chemical Engineering, Kansas State University, Manhattan, KS, USA. [2]Shared Instrumentation Facility, Colorado School of Mines, Golden, CO, USA. [3]Department of Materials, Imperial College London, Exhibition Road, London SW7, UK. [4]Nissan Technical Center North America (NTCNA), Farmington Hills, MI, USA. [5]Nissan Research Center, Nissan Motor Company Limited, Yokosuka, Kanagawa, Japan. [6]School of Aerospace and Mechanical Engineering, University of Oklahoma, Norman, OK, USA. [7]Department of Mechanical Engineering, University of Kansas, Lawrence, KS, USA. [8]Department of Chemical Engineering, University of Utah, Salt Lake City, UT, USA.
*Corresponding author. Email: c.duan@utah.edu

Downloaded from https://www.science.org at Imperial College London on January 16, 2025

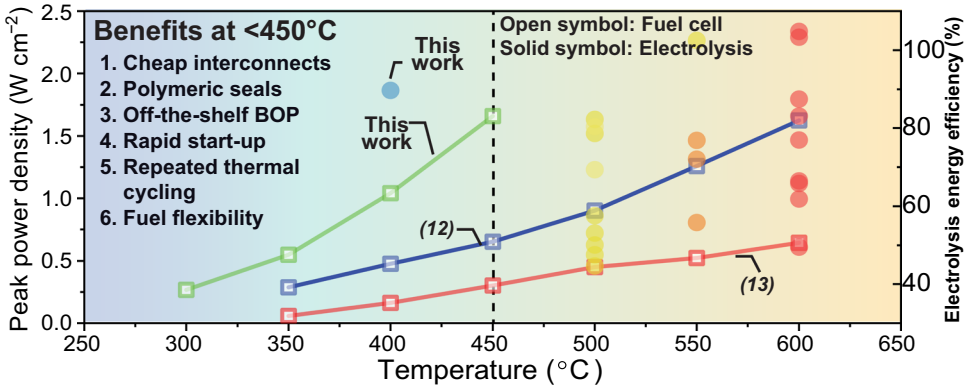


Fig. 1. Motivation for lowering the operating temperature of PCECs to <450°C. Solid symbols, PCEC electrolysis energy efficiencies (EEE) as a function of operating temperature at a H_2 production rate of 0.03 to 0.05 ml cm^{-2} s^{-1}. Open symbols, PCEC fuel cell peak power densities as a function of operating temperatures. The green square open symbols present the PCEC fuel cell performance demonstrated in this work (cell 1). The blue round solid symbols present the PCEC EEE demonstrated in this work (cell 2). The blue square open symbols show one of the state-of-the-art PCECs (*12*). The red square open symbols correspond to the PCECs previously designed by Duan *et al.* (*13*). The rest of the solid symbols display the literature results regarding PCEC EEE (table S1) (*12*, *30*, *32*, *33*, *51*–*55*).

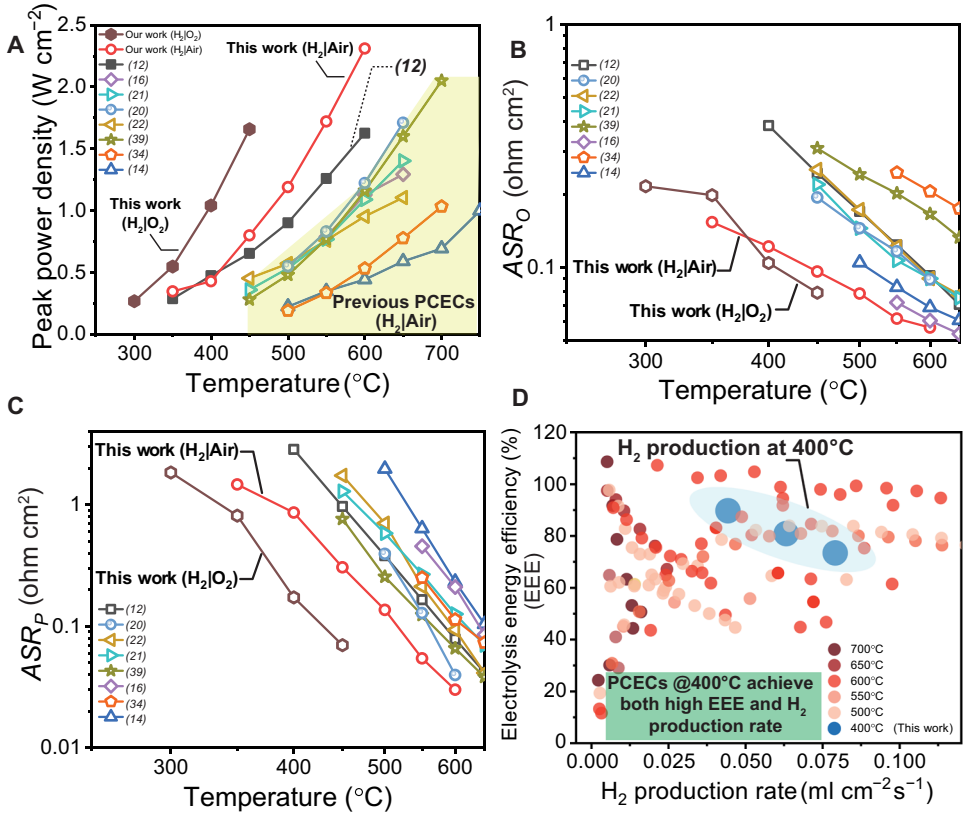


Fig. 2. Comparison of UHP LT-PCECs and other PCECs. (**A**) Comparison of fuel cell peak power densities with literature results. This work (H_2|O_2, cell 1); this work (H_2|Air, cell 3); Ding (H_2|O_2) (*12*); Liu (H_2|Air) (*20*); Lee (H_2|Air) (*22*); Haile (H_2|Air) (PLD) (*21*); Duan (H_2|Air) (*13*); Park (H_2|Air) (*39*); Shim (H_2|Air) (*16*); Shao (H_2|Air) (*34*); Lee (H_2|Air) (*14*). (**B**) Comparison of ASR_O in PCEC fuel cell mode with literature results. (**C**) Comparison of ASR_P in PCEC fuel cell mode with literature results. (**D**) PCEC electrolysis energy efficiency as a function of H_2 production rate at 400° to 700°C. Comparison of this work (cell 2) with literature results (table S1). Some PCECs achieve an electrolysis energy efficiency of >100% as free waste heat can be used for hydrogen production during the endothermic operation.

Downloaded from https://www.science.org at Imperial College London on January 16, 2025

fabrication processes, an optimized pairing of the Ba-rich negative electrode ($BaCe_{0.7}Zr_{0.1}Y_{0.1}Yb_{0.1}O_{3-\delta}$ + NiO) and electrolyte ($BaCe_{0.4}Zr_{0.4}Y_{0.1}Yb_{0.1}O_{3-\delta}$) minimizes the Ba deficiency in electrolyte layer, which improves the electrolyte densification, increases its grain size, and readily produces single-grain–thick and chemically homogeneous electrolytes, consequently reducing the ohmic area–specific resistance (ASR_O) to 0.08 ohm·cm^2 on H_2 fuel at 450°C (versus, e.g., 0.2 to 0.6 ohm·cm^2 at 450°C for previous PCECs; Fig. 2B). Second, the nano-micro positive electrode ($BaCo_{0.4}Fe_{0.4}Zr_{0.1}Y_{0.1}O_{3-\delta}$ + $BaCe_{0.4}Zr_{0.4}Y_{0.1}Yb_{0.1}O_{3-\delta}$) decreases the coefficient of thermal expansion (CTE), leads to microparticles reinforced composite electrode, and enhances the positive electrode-electrolyte interfacial bonding, further reducing ASR_O. Moreover, the nano-micro positive electrode creates well-connected proton conduction channels, thereby improving the electrocatalytic activity (Fig. 2C) and achieving an unprecedentedly low ASR_P.

This set of approaches leads to exceptional hydrogen fuel cell performance at 300° to 450°C with peak power densities of 0.2 to 1.6 W cm^{-2} (Fig. 2A) and stable steam electrolysis performance with both high electrolysis energy efficiency and high H_2 production rate at 400°C (Fig. 2D), which outperform the literature results (*1*, *2*, *12*–*16*, *20*–*23*). Figures 1 and 2D shows that the UHP LT-PCECs achieve an electrolysis energy efficiency and a H_2 production rate comparable to or even higher than those of previous PCECs that operate at 500° to 700°C. At 400°C, the PCECs achieve a high Faradaic efficiency of >90% at a current density of 0.6 A cm^{-2}. Furthermore, reducing the temperature does not sacrifice the fuel flexibility of these ceramic fuel cells. We demonstrate that the PCECs can directly use ammonia and methane for power generation at <450°C with excellent performance. The appropriate electrolyte-negative electrode pair creates chemically homogeneous electrolyte, which enhances the electrolyte robustness under harsh conditions, enabling long-term durable operation on ammonia fuel without the use of any additional catalysts. The UHP LT-PCECs also demonstrate long-term (>2000 hours) durability in steam electrolysis mode at 400°C, which highlights the promise of PCECs for H_2 production at 400°C.

Readily fabricated single-grain–thick, chemically homogeneous, and low-resistant electrolyte

$BaCe_{0.4}Zr_{0.4}Y_{0.1}Yb_{0.1}O_{3-\delta}$ (BCZYYb4411) and $BaCe_{0.7}Zr_{0.1}Y_{0.1}Yb_{0.1}O_{3-\delta}$ (BCZYYb7111) have been designed to enhance the intrinsic proton conductivity (*21*, *24*). Nevertheless, PCECs that use either BCZYYb4411 or BCZYYb7111 achieve highly disparate conductivities (fig. S3). These variations could be attributed to the different intrinsic electrolyte conductivity, contact resistance, and ohmic resistance of the electrodes. As shown in Fig. 3 (A to D), we recognize that the pairing of the same electrolyte and different negative electrodes can affect the microstructure, chemical composition, and conductivity of the electrolyte; thus, modulating the electrolyte-negative electrode pair is critical, which is typically ignored during the PCEC design and fabrication processes (*25*).

We studied the pairing of the same electrolyte (BCZYYb4411) with negative electrodes fabricated via two approaches. Solid-state reactive sintering (SSRS) was pioneered to lower the PCEC sintering temperature (*13*, *26*). Although high performance has been obtained, further improvement is hampered by the relatively low electrolyte conductivity. When the BCZYYb4411 electrolyte is paired with the BCZYYb7111+NiO negative electrode processed via SSRS (electrolyte 2, Supplementary Methods; Fig. 3B and fig. S4), the electrolyte is multiple-grains thick (fig. S5), leading to high grain boundary resistance and ASR_O. Alternatively, the same electrolyte paired with a BCZYYb7111+NiO negative electrode fabricated via the solid-state sintering (SSS) process exhibits the desired single-grain–thick structure (electrolyte 1; Fig. 3A), which reduces the grain boundary resistance. Moreover, the BCZYYb4411 electrolyte paired with a BCZYYb7111+NiO (SSS) negative electrode has a 2.0-fold increase in the grain size over the same electrolyte coated on a BCZYYb7111+NiO (SSRS) negative electrode (Fig. 3, C and D).

Figures S6 and S7 show energy-dispersive x-ray spectroscopy (EDS) results used to determine the chemical composition of the electrolytes. As shown in Fig. 3 (C and D), fig. S8, and tables S2 and S3, electrolyte 1 was found to contain 49.4 atomic % (at. %) Ba, which is close to the theoretical concentration (49.0 at. %) of Ba. However, electrolyte 2 contains a lower Ba concentration (46.9 at. %), leading to a relatively high Ba deficiency (2.1%). Therefore, using the BCZYYb7111+NiO (SSS) negative electrode can help achieve a stoichiometric electrolyte with minimized Ba deficiency, which is essential for electrolyte densification and grain growth (*14*).

The ASR_O measurements at 500°C, as shown in fig. S9, indicate that the BCZYYb7111+NiO (SSS) negative electrode enables a decrease in the ASR_O from 0.25 to 0.09 ohm·cm^2 compared to the BCZYYb7111+NiO (SSRS) negative electrode. In addition, the activation energy is reduced, which is beneficial for lowering the PCEC operating temperature. The enhanced property is mainly due to a smaller grain boundary area, a larger grain size, a lower porosity, and less Ba deficiency (Fig. 3, A and C). Therefore, the BCZYYb4411 electrolyte-BCZYYb7111+NiO (SSS) negative electrode can provide better PCEC performance. Various PCECs with this favorable paring were characterized to demonstrate the reproducibility (fig. S10). A single-grain–thick electrolyte with a thickness of ~5 μm can be readily processed via this multilayer co-sintering process. All PCECs fabricated with this electrolyte exhibit high reliability and reproducibility (table S4). Therefore, these PCECs are scalable and low cost for large-scale production. Hydrogen pumping experiments were conducted to demonstrate that this single-grain–thick electrolyte does not exhibit n type electronic or mechanical leakage (fig. S11).

Transmission electron microscopy (TEM) images also show that the electrolyte paired with a BCZYYb7111+NiO (SSS) negative electrode displays the single-grain–thick structure (Fig. 3E). EDS images (figs. S12 and S13) show the cation distributions and chemical compositions of electrolyte 1 and electrolyte 2, which indicate that all constituent cations are uniformly distributed throughout the electrolytes, suggesting no notable elemental depletion or segregation on the micron scale. In contrast, high-magnification high-angle annular dark field (HAADF) imaging and EDS mapping of the grain boundaries in electrolytes 1 and 2 reveal noticeable differences (Fig. 3, F and G). The EDS thermal color palette images of all cations in electrolyte 2 across the grain boundary show that Yb segregation occurs at the grain boundary (Fig. 3G). As illustrated in Fig. 3H, we hypothesize that the Yb segregation could be attributed to the Ba deficiency (*14*). The BCZYYb7111+NiO (SSRS) negative electrode leads to electrolyte 2 with a high Ba deficiency, driving the Yb segregation along the grain boundary. As the Yb concentration is 10 mol % while the Ba concentration is 10 times that of Yb, a minor Ba depletion can lead to significant Yb segregation along the grain boundary. Yb doping is critical for the high proton conductivity and stability of BCZYYb (*24*). In addition, Yb segregation could also lead to a positively charged grain boundary core, causing the proton depletion at the grain boundary, which reduces the electrolyte conductivity (*27*–*29*). Considering that electrolyte 1 exhibits a smaller

Downloaded from https://www.science.org at Imperial College London on January 16, 2025

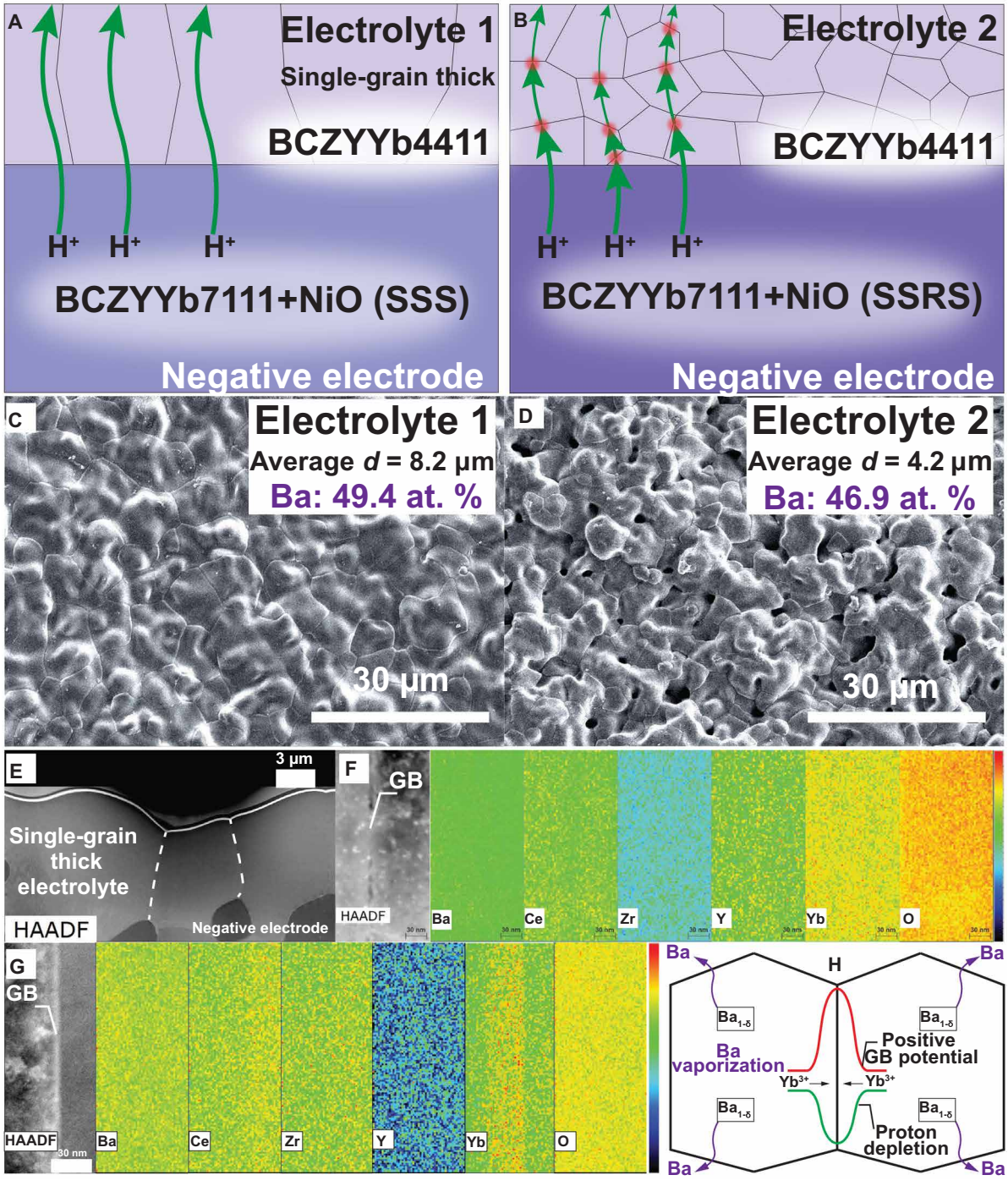


Fig. 3. Redesigned electrolyte-negative electrode pair to readily fabricate single-grain–thick and chemically homogeneous electrolyte. (**A**) Pairing the BCZYYb4411 electrolyte and a BCZYYb7111+NiO (SSS) negative electrode leads to a thin, large-grain, and single-grain–thick electrolyte via the simple cosintering process (electrolyte 1). These thick green arrows show the proton conduction with low resistance; thus, electrolyte 1 has high proton conductivity. (**B**) Pairing the BCZYYb4411 electrolyte and a BCZYYb7111+NiO (SSRS) negative electrode produces a thin, small-grain, and multiple-grains–thick electrolyte (electrolyte 2). These green arrows show the proton conduction with resistance at the grain boundaries; thus, electrolyte 2 has lower proton conductivity than electrolyte 1. (**C**) The SEM image of electrolyte 1 surface, average grain size, and Ba concentration. The Ba concentration was determined using the EDS results shown in fig. S6 and table S2 (cell 4). (**D**) The SEM image of electrolyte 2 surface, average grain size, and Ba concentration. The Ba concentration was determined using the EDS results shown in fig. S7 and table S3 (cell 5). (**E**) HAADF-STEM image of PCEC with electrolyte 1, which shows the single-grain thick electrolyte (cell 6). (**F**) HAADF image of the grain boundary in electrolyte 1 and the corresponding EDS mapping of Ba, Ce, Zr, Y, Yb, and O (cell 6). (**G**) HAADF image of the grain boundary in electrolyte 2 (cell 7) and the corresponding EDS mapping of Ba, Ce, Zr, Y, Yb, and O (cell 7). The scale bars in (F) and (G) show concentration of elements, where the black indicates the lowest concentration while red displays the highest concentration. Not all the elements are on the same scale. (**H**) Proposed mechanism of Ba deficiency and Yb segregation and their impacts on proton conductivity.

Downloaded from https://www.science.org at Imperial College London on January 16, 2025

grain boundary area and a more uniform cation distribution than electrolyte 2, pairing the BCZYYb4411 electrolyte with a BCZYYb7111+NiO (SSS) negative electrode can construct PCECs with minimized ASR_O.

The impact of negative electrodes on electrolyte microstructure and chemical composition

The densification and grain growth of electrolytes can also be affected by PCEC shrinkage. However, these two kinds of PCECs show opposite trends of the shrinkage rate; thus, the discrepancy in electrolyte properties is not due to the shrinkage (table S5). As Fig. 3 (C and D) shows that electrolyte 1 and electrolyte 2 have different Ba concentrations, we hypothesize that the distinct electrolyte properties are ascribed to elemental diffusion across the electrolyte-negative electrode interface. To validate this hypothesis, electrolyte sintering experiments and comprehensive characterizations were conducted by sintering the same BCZYYb4411 dry-pressed pellets (1 mm thick) on setters made of two different negative electrode materials and alumina (Fig. 4; experimental details are provided in Materials and Methods), eliminating the impacts of negative electrode shrinkage on the electrolyte sintering. These tests showed consistent results with the PCEC half cells (fig. S14 and Fig. 3, A to D). Pairing BCZYYb4411 with a BCZYYb7111+NiO (SSS) negative electrode leads to the lowest porosity and largest grain size. Figure 4 (A to C) also shows the grain size gradient across the electrolyte membrane. Larger grains and a higher density are observed at the side contacting the negative electrode setters (Fig. 4A). Using the alumina as the setter (Fig. 4C), BCZYYb4411 shows a porous microstructure with very small grains. These results indicate that electrolyte densification and grain growth hinge on elemental diffusion at the electrolyte-negative electrode interface.

The scanning electron microscope (SEM)–EDS results in Fig. 4 (D to F) and figs. S15 to S20, and tables S6 to S11 indicate that using negative electrode substrates as setters can help to maintain Ba stoichiometry in the electrolyte, which is crucial for producing dense, large-grain, chemically uniform, and highly conductive electrolytes (*14*). Figure 4D shows that pellet 1 has an average Ba concentration of 48.6 at. % on the contact side, close to the theoretical value (49.0 at. %) and the Ba concentration in PCEC electrolyte (electrolyte 1; Fig. 3C). In addition, the contact side of pellet 2 has a Ba concentration of 44.8 at. % (Fig. 4E), which is also close to the Ba concentration in PCEC electrolyte (electrolyte 2; Fig. 3D). In contrast, pellet 3 sintered on an alumina setter has a lower Ba concentration (44.0 at. %; Fig. 4F). This confirms that negative electrodes can act as Ba reservoirs, supplying Ba to the electrolyte layer and mitigating Ba deficiency resulting from inevitable Ba vaporization during sintering (Fig. 4, A to C). Figure 4D also shows that Ba diffuses from the negative electrode substrate to the electrolyte layers, as evidenced by the Ba concentration gradient across pellet 1, which shows that the contact side has a higher Ba concentration than the top side.

Further analyses show that the fully crystallized BCZYYb7111+NiO (SSS) negative electrode (Ba: 49.8 at. %) has a higher available Ba content than the BCZYYb7111+NiO (SSRS) negative electrode (Ba: 48.1 at. %; figs. S21 and S22 and tables S12 and S13). Using the BCZYYb7111+NiO (SSS) negative electrode provides more Ba to the electrolyte, promoting grain growth and reducing Ba deficiency, resulting in improved chemical homogeneity and proton conductivity (Fig. 3A). However, the BCZYYb7111+NiO (SSRS) cannot provide a positive net amount of Ba, leading to a lower Ba concentration at the contact side and negligible Ba concentration gradient (Fig. 4E). In contrast, the alumina setter acts as a strong Ba absorber, which reduces the Ba concentration at the contact side, resulting in an opposite Ba concentration gradient compared to pellet 1 (Fig. 4F). Caution is warranted regarding the employment of alumina setter for high-temperature sintering (>1450°C) in PCEC manufacturing. The ceramic phase (BCZYYb7111) in BCZYYb7111+NiO (SSS) negative electrodes were pre-sintered and fully crystallized during a fast-heating step (10°C/min), which allows to better trap Ba in the lattice and prevent significant Ba loss before electrolyte densification (fig. S23). This fast-heating pre-sintering step establishes the SSS negative electrode as a Ba reservoir, directly supplying Ba to the electrolyte during the high-temperature co-sintering process. This continuous Ba source from the negative electrode helps maintain electrolyte stoichiometry, resulting in large grain size, low grain boundary area, chemically homogeneous grain boundary, and improved proton conductivity. In contrast, the SSRS negative electrode, not subjected to pre-crystallization, undergoes simultaneous crystallization and densification with the electrolyte during the high-temperature processes (fig. S23). The Ba tends to vaporize at temperatures that are lower than the electrolyte densification temperature. In addition, the co-sintering process is a slow heating process (e.g., 1° to 2°C/min). Therefore, significant Ba can vaporize from the negative electrode before electrolyte densification. SSRS negative electrode will not effectively serve as the Ba reservoir.

To summarize, the proposed SSS-processed negative electrode presents a straightforward and easily scalable method to improve the densification and proton conductivity of the electrolyte. The pre-crystallization of BCZYYb7111 in the SSS negative electrode eliminates the need for external Ba sources during the sintering process, making the entire process more accessible, straightforward, and cost effective.

Improved electrochemical performance and positive electrode-electrolyte interfacial bonding with nano-micro positive electrode

The second major reason why PCECs perform poorly at 300° to 450°C is the lack of a highly active positive electrode deliberately designed for UHP LT-PCECs. The oxygen reduction reaction (ORR) and oxygen evolution reaction (OER) are sluggish processes. Therefore, by reducing the operating temperature, ASR_P, i.e., the area-specific positive electrode polarization resistance, tends to dominate the total resistance (fig. S2). Positive electrodes, including $BaCo_{0.4}Fe_{0.4}Zr_{0.1}Y_{0.1}O_{3-\delta}$ (BCFZY) (*13*, *30*, *31*), $PrBa_{0.5}Sr_{0.5}Co_{1.5}Fe_{0.5}O_{5+\delta}$ (PBSCF) (*21*), $PrNi_{0.5}Co_{0.5}O_{3-\delta}$ (PNC) (*32*), $Ba_{1-x}Gd_{0.8}La_{0.2+x}Co_2O_{6-\delta}$ (BGLC) (*33*), and $Na_xCa_{3-x}Co_4O_{9-\delta}$ (*18*) have been demonstrated to achieve remarkable PCEC performance at 500° to 600°C. However, their electrocatalytic activity is still low at 300° to 450°C, necessitating the design of alternative positive electrodes. The concept of a composite electrode was thereby proposed. Although the enhanced performance was validated at 500° to 600°C, its beneficial contribution to improving the PCEC performance at 300° to 450°C was insignificant (*34*, *35*).

We developed a composite electrode composed of a nanosized mixed ionic and electronic conductor (MIEC, BCFZY) and a microsized proton conductor (BCZYYb4411), called the nano-micro positive electrode (Fig. 5C and figs. S24 and S25). We also studied single-phase nanosized BCFZY, denoted the nano positive electrode (Fig. 5A and fig. S26). Alternatively, a composite of a nanosized MIEC (BCFZY) and a nanosized proton conductor (BCZYYb4411) was also characterized in this work, named the nano-nano positive electrode (Fig. 5B and fig. S27). The Brunauer-Emmett-Teller surface area of nanosized BCFZY, nanosized BCZYYb4411, and microsized BCZYYb4411 before and after sintering was listed in table S14. The performance of PCECs equipped with these three kinds of positive electrodes

Downloaded from https://www.science.org at Imperial College London on January 16, 2025

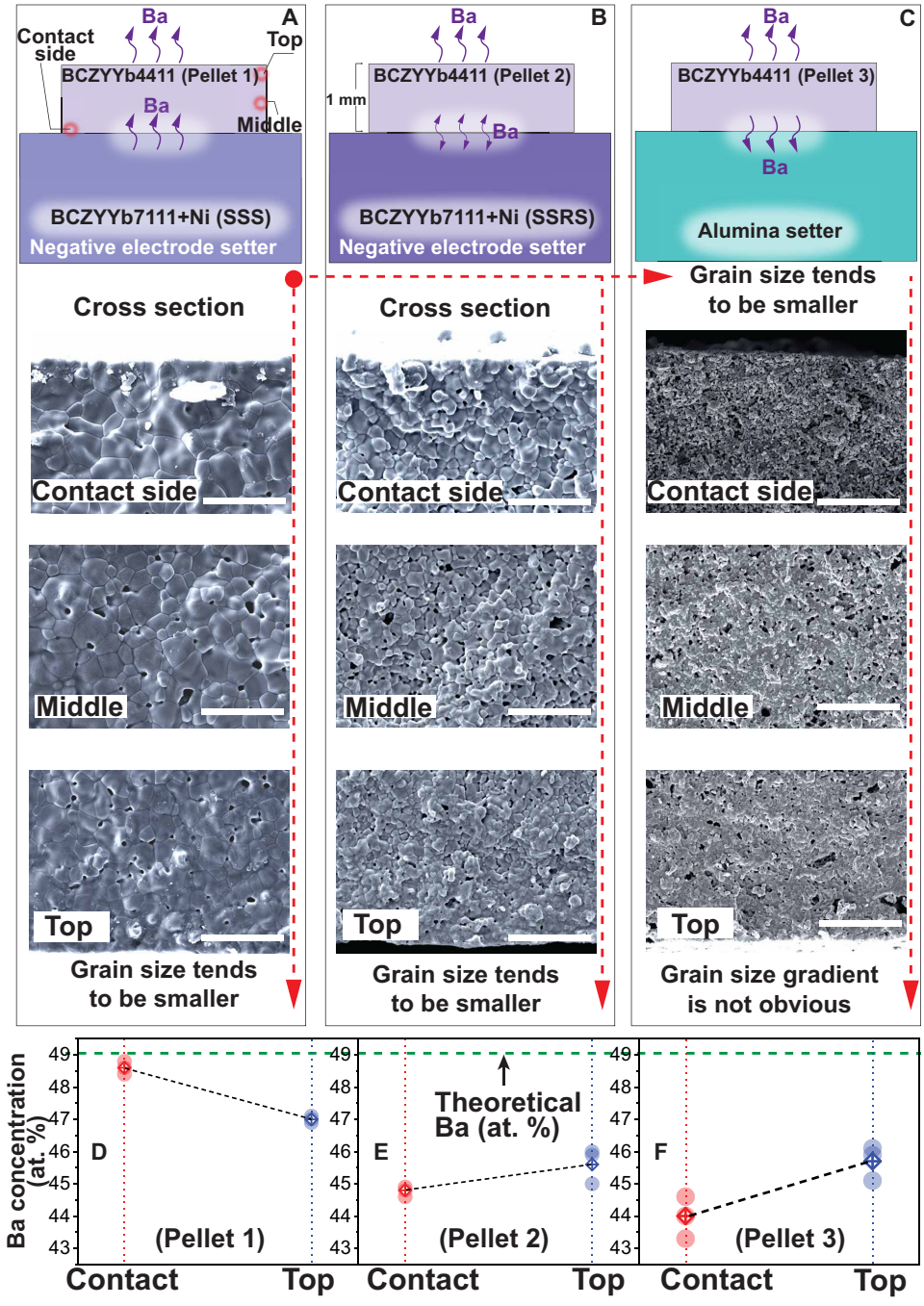


Fig. 4. Impacts of negative electrode setters on the microstructure and chemical composition of the same BCZYYb4411 electrolyte pellets, which have a thickness of 1 mm. Scale bar, 20 μm. (**A**) Sintering the BCZYYb4411 dry-pressed pellet (pellet 1) on the BCZYYb7111+NiO (SSS) negative electrode setter. (cell 8) (**B**) Sintering the BCZYYb4411 dry-pressed pellet (pellet 2) on the BCZYYb7111+NiO (SSRS) negative electrode setter. (cell 9) (**C**) Sintering the BCZYYb4411 dry-pressed pellet (pellet 3) on the alumina setter. (cell 10). The SEM images of the electrolyte surface that contacts the setters show that the BCZYYb7111+NiO (SSS) negative electrode setter leads to the largest grain size. In addition, using the alumina setter achieves the smallest grain size, indicating that the negative electrode can promote the electrolyte dentification and grain growth. In this experiment, the dry-pressed pellets are placed on the setters, which are not constrained by the setters, ruling out the impact of the setter shrinkage on electrolyte densification and grain growth. Furthermore, the cross-sectional SEM images clearly display that the contact side exhibits high density and large grains, while the top side shows relatively small grains and low density, confirming that the electrolyte densification and grain growth hinge on the elemental diffusion. (**D**) The Ba concentration of the contact side and top side of pellet 1. (**E**) The Ba concentration of the contact side and top side of pellet 2. (**F**) The Ba concentration of the contact side and top side of pellet 3.

Downloaded from https://www.science.org at Imperial College London on January 16, 2025

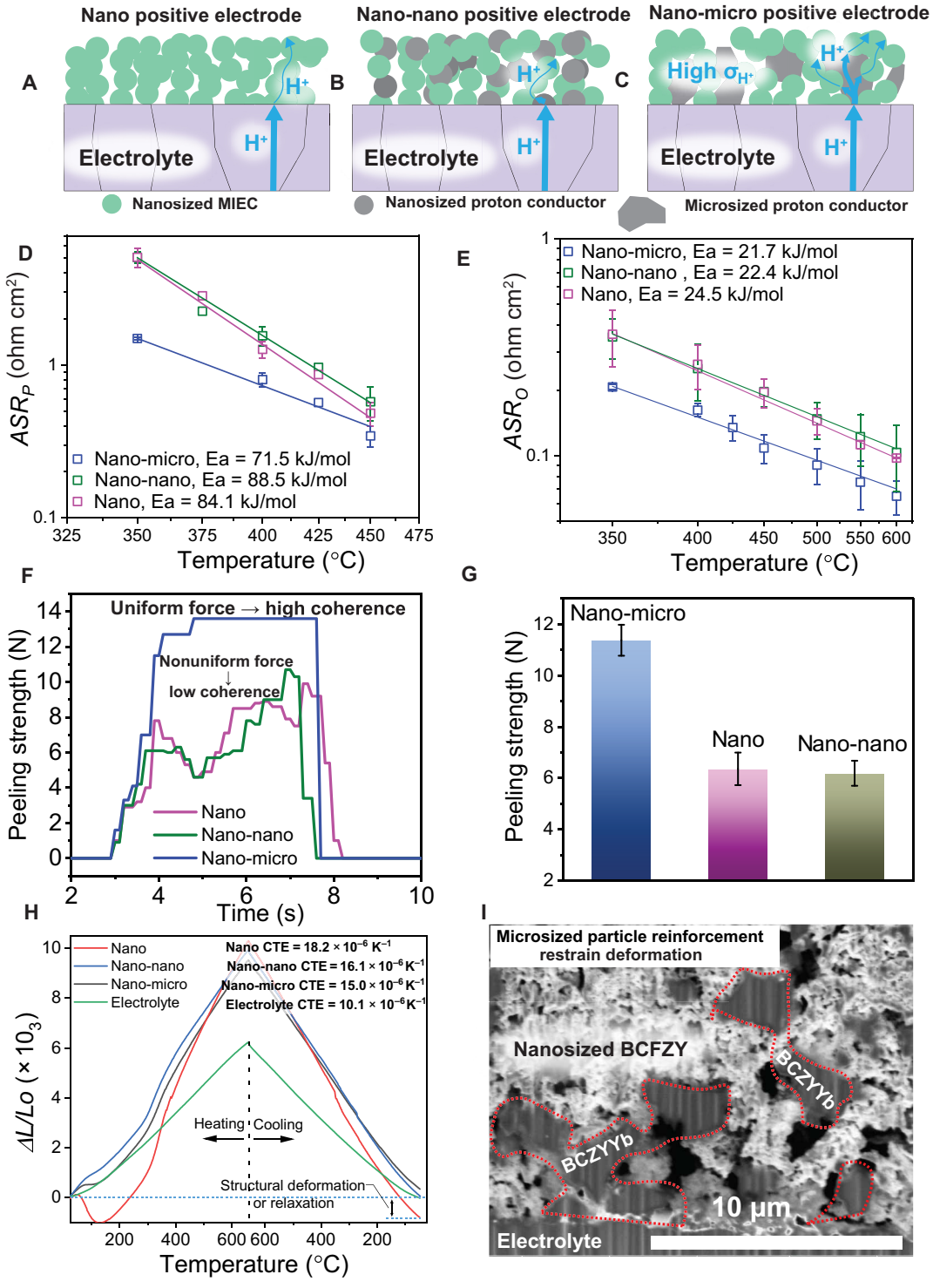


Fig. 5. Redesigned nano-micro positive electrode simultaneously reducing ASR_O and ASR_P. The errors bars in these figures correspond to SDs from the averaging across all measurements. (**A**) Illustration of the nano positive electrode, which is a nanosized $BaCo_{0.4}Fe_{0.4}Zr_{0.1}Y_{0.1}O_{3-\delta}$ (BCFZY). (**B**) Illustration of the nano-nano positive electrode, which is a composite of a nanosized BCFZY and a nanosized $BaCe_{0.4}Zr_{0.4}Y_{0.1}Yb_{0.1}O_{3-\delta}$ (BCZYYb). (**C**) Illustration of the nano-micro positive electrode, which is a composite of a nanosized BCFZY and a microsized BCZYYb. (**D**) The ASR_P of PCECs is equipped with three kinds of positive electrodes shown in (A) to (C). All results are measured in fuel cell mode and under OCV condition (cell 3 and cells 11 to 15). (**E**) The ASR_O shown in (A) to (C). (**F**) Examples of peeling strength measurement plots for three positive electrodes (cell 16). (**G**) Peeling strength of electrolyte-positive electrode interface (cells 16 to 18). (**H**) Linear thermal expansion of three positive electrodes as a function of temperature during heating and cooling, and corresponding thermal expansion coefficients (TECs) (nano, cell 19; nano-nano, cell 20; nano-micro, cell 21). (**I**) SEM image of the nano-micro positive electrode, which shows how the microsized phase functions as particle reinforcement to restrain the structural deformation.

Downloaded from https://www.science.org at Imperial College London on January 16, 2025

reveals that the nano-micro positive electrode simultaneously reduces ASR_P and ASR_O (Fig. 5, D and E, and figs. S28 to S34).

As shown in Fig. 5C and figs. S35 and S36, the micro proton-conducting oxide phase serves as an effective proton conduction channel and reinforcement, enhancing the proton conductivity and electrocatalytic activity of the electrode while improving its microstructural stability and compatibility with the electrolyte. Our results show that, unlike the conventional nano-nano positive electrode, the "rationally designed" nano-micro phase operates as a triple conducting oxide positive electrode (figs. S33 and S34), creating a network that facilitates proton conduction, which effectively increases the electrochemically active sites for both OER and ORR. In contrast, the nanosized proton–conducting phase in the nano-nano positive electrode cannot effectively build a proton conduction channel as this phase is dispersed in the nanosized MIEC phase (Fig. 5B and fig. S35B), which does not obviously improve the electrocatalytic activity. Thus, the nano-micro positive electrode reduces the ASR_P.

The nano-micro positive electrode improves the strength and coherence of the electrolyte-positive electrode interfacial bonding, leading to a peeling strength of 11.4 N (Fig. 5, F and G, and fig. S37), which is much higher than those of the nano positive electrode (6.4 N) and the nano-nano positive electrode (6.1 N). Improving the interfacial bonding reduces the contact resistance, which is consistent with the ASR_O shown in Fig. 5E (*12*). The nano-nano positive electrode displays the similar interfacial bonding with that of nano positive electrode; thus, the ASR_O of the PCEC with the nano-nano positive electrode is comparable to that for the nano positive electrode. Therefore, the PCECs with nano-micro positive electrodes attain the lowest ASR_O (Fig. 5E). Figure 5E shows that the activation energy decreases when using the nano-micro positive electrode, indicating that both the preexponential factor and the mechanisms of electrode reactions at the interface are changed (text S1).

Moreover, the dilatometry results (Fig. 5H) indicate that the nano-micro positive electrode has the closest linear expansion profile with the electrolyte, while the profile of the nano positive electrode deviates. We also found that the nano-micro electrode has a lower CTE ($15.0 \times 10^{-6}\ K^{-1}$) than the conventional nano positive electrode ($18.2 \times 10^{-6}\ K^{-1}$) and the nano-nano composite positive electrode ($16.1 \times 10^{-6}\ K^{-1}$), which improves the electrolyte-positive electrode compatibility and interfacial bonding (*36*). In addition, the dilatometry results of the nano positive electrode indicate that it shows deformation or structural relaxation upon one thermal cycle, which is detrimental to the interfacial adherence. It is widely recognized that large particles in ceramic composites can restrain structural deformation, prevent the initiation or propagation of cracks, and improve toughness (*37*, *38*). As displayed in Fig. 5I and fig. S38, we hypothesize that the microsized particles in the nano-micro electrode function as particle reinforcements, which are similar to the stones in concrete, restraining the crack initiation and propagation in the positive electrode (*37*, *38*). Therefore, the mechanical integrity of the electrode-electrolyte interfaces is improved with the nano-micro positive electrodes and there are fewer cracks at the interfaces.

In summary, the nano-micro positive electrode can achieve improved electrochemical performance and enhanced interfacial bonding. The reduced activation energy is due to a combination of two main factors, including effective proton-conduction channels created by the micro phase and the enhanced electrolyte-positive electrode interfacial bonding, which is also consistent to the distribution of relaxation time analyses (fig. S39 and text S4). At 350°C, ASR_P decreases from 5.1 to 1.5 ohm·cm^2 upon changing the nano positive electrode to the nano-micro positive electrode. The PCEC performance shown in fig. S40 implies that the nano-micro positive electrode results in a 3.1-fold increase in the fuel cell peak power density at 350°C.

UHP LT-PCECs for power generation at <450°C

Combining the appropriate electrolyte-negative electrode pair with the nano-micro positive electrode allows us to redesign UHP LT-PCECs (fig. S41). The open-circuit voltages (OCVs) for all PCECs under fuel cell operation are higher than 1.05 V (fig. 6, A and B), indicating that the single-grain–thick electrolyte exhibits negligible electronic and mechanical leakage. Compared to our previous-generation PCECs, the redesigned PCECs achieve much higher fuel cell performance (Fig. 6C and figs. S42 and S43). With air as the feedstock to the positive electrode, a superior peak power density of 2.2 W cm^{-2} is reached at 600°C (Fig. 6A), which outperforms the reported PCEC fuel cell results in the literature (Fig. 2A) (*12*–*14*, *16*, *20*–*22*, *34*, *39*). To compare the UHP LT-PCEC with the state-of-the-art PCECs (*12*), oxygen was fed to the positive electrode, and a peak power density of 1.6 W cm^{-2} is achieved at 450°C (Fig. 6B). Previously reported power densities at 450°C typically range from 0.2 to 0.7 W cm^{-2} (Fig. 2A). In addition, we have demonstrated PCEC operation at 300°C, delivering a viable fuel cell peak power density of 0.2 W cm^{-2} on H_2-O_2 (Fig. 6B). At 450°C, these readily processed PCECs with a redesigned architecture offer a more than threefold increase in the fuel cell performance compared to PCECs with acid-etched electrolytes and three-dimensional positive electrodes (Fig. 2A).

The UHP LT-PCECs operating at 300° to 450°C also exhibit good fuel flexibility. The fuel cell performance was evaluated on ammonia and methane fuel. On ammonia fuel, without applying any catalysts, the UHP LT-PCECs offer peak power densities of 0.5 W cm^{-2} at 450°C, 0.25 W cm^{-2} at 400°C, and 0.15 W cm^{-2} at temperatures as low as 350°C (Fig. 6D and fig. S44). At 450°C, the performance of the UHP LT-PCECs on ammonia fuel can still reach ~65% on H_2 fuel (fig. S45), indicating that the negative electrode is active for ammonia cracking, which suggests that ammonia could serve as a H_2 carrier for power generation in PCECs. The direct-ammonia PCECs also attain outstanding performance at 600° to 500°C, achieving a peak power density of 1.7 W cm^{-2} at 600°C (fig. S46), which greatly exceeds the results reported in the literature (Fig. 6E).

In addition, the UHP LT-PCECs can directly use methane for power generation (Fig. 6F and figs. S47 and S48). At 500°C, as shown in Fig. 5F, we demonstrate a peak power density of 0.8 W cm^{-2} on methane fuel [versus, e.g., 0.55 W cm^{-2} at 500°C (*40*) and 1.2 W cm^{-2} at 650°C for previous intermediate-temperature solid oxide fuel cells (*41*)], which approaches the performance of PCECs on pure H_2 fuel (fig. S48). The *I-V* performance of the PCECs on methane fuel shows that a viable peak power density can still be produced at 400°C, implying that direct PCEC operation on natural gas at <400°C is feasible.

UHP LT-PCECs for hydrogen production at <450°C

We also investigated the PCECs in steam electrolysis mode for hydrogen production at <450°C (texts S2 and S3). As shown in Fig. 6H, the redesigned UHP LT-PCECs attain a current density of 1.15 A cm^{-2} at 1.4 V and 450°C [versus, e.g., 1.04 A cm^{-2} at 450°C for the state-of-the-art PCECs (*12*)]. Furthermore, Fig. 6I and fig. S47 shows that the PCECs achieve reasonable Faradaic efficiency (FE% > 85% at 400°C). At

Downloaded from https://www.science.org at Imperial College London on January 16, 2025

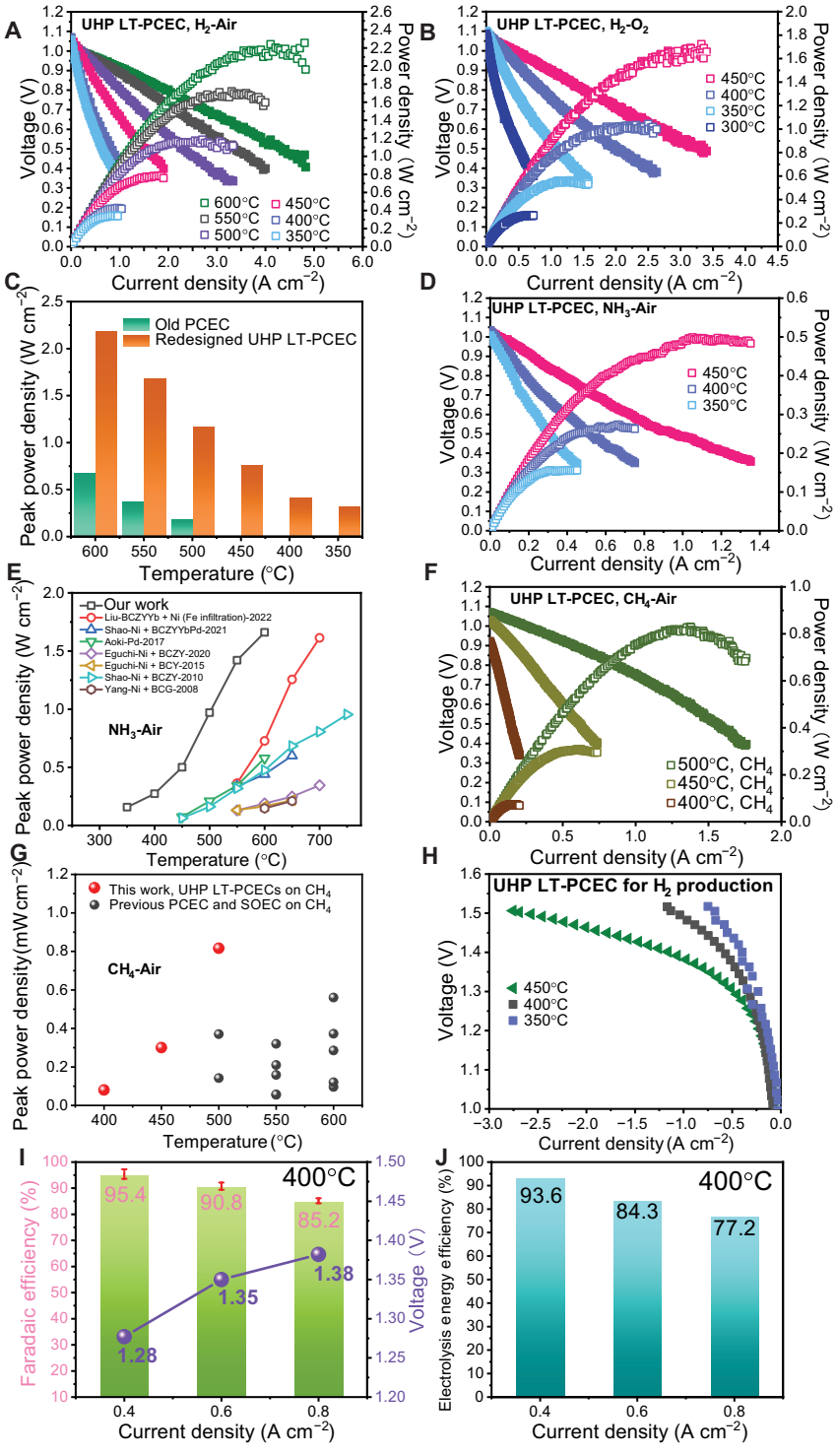


Fig. 6. Exceptional performance of redesigned UHP LT-PCECs in both fuel cell and steam electrolysis modes. The errors bars in these figures correspond to SDs from the averaging across all measurements. (**A**) Polarization and power density curves of a representative UHP LT-PCEC with the redesigned architecture at 350° to 600°C (cell 3). H_2 is fed to the negative electrode and air is fed to the positive electrode. (**B**) Polarization and power density curves of a representative UHP LT-PCEC with the redesigned architecture at 300° to 450°C. H_2 is fed to the negative electrode, and O_2 is fed to the positive electrode (cell 1). (**C**) Comparison of UHP LT-PCEC fuel cell performance (cell 3) with the old PCEC (cell 22). (**D**) Polarization and power density curves of a representative UHP LT-PCEC on ammonia fuel at 300° to 450°C. NH_3 is fed to the negative electrode, and air is fed to the positive electrode (cell 23). (**E**) Comparison of UHP LT-PCEC fuel cell performance on ammonia fuel with literature results (*42*–*48*). (**F**) Polarization and power density curves of a representative UHP LT-PCEC on methane fuel at 400° to 500°C. Methane fuel stream is fed to the negative electrode, and air is fed to the positive electrode (cell 24). (**G**) Comparison of UHP LT-PCEC fuel-cell performance on methane fuel with literature results (*13*, *40*, *41*, *49*, *56*–*66*). (**H**) Polarization curves of a representative UHP LT-PCEC in electrolysis mode at 350° to 450°C. 40% H_2O + 60% N_2 is fed to the positive electrode (cell 25). (**I**) Faradaic efficiency of the UHP LT-PCEC at 400°C (cell 2). (**J**) Electrolysis energy efficiency of the UHP LT-PCEC at 400°C (cell 2).

Downloaded from https://www.science.org at Imperial College London on January 16, 2025

400°C and a current density of 0.6 A cm^{-2}, the cell-level electrical energy-to-chemical energy conversion efficiency reaches 84.3% (Fig. 6J), highlighting the promise of low-cost H_2 production in PCECs at 400°C.

Stability of UHP LT-PCECs for power generation and hydrogen production

We then performed stability testing of our UHP LT-PCECs for both power generation and hydrogen production at <450°C. At a practical current density of 400 mA cm^{-2} and 400°C, the PCEC continuously operates in fuel cell mode for over 400 hours, achieving a degradation rate of <0.01 mV/100 hours (Fig. 7A). The electrochemical impedance spectroscopy plots during the stability test show that both the electrolyte and electrode are stable (Fig. 7B). After the stability test, there is no observable change in the microstructure and no electrolyte crack (fig. S50). The electrolyte-electrode interfaces show no delamination, suggesting that the interfacial bonding is good, and the thermal expansions are compatible.

Long-term stability test data of the UHP LT-PCECs for H_2 production in steam electrolysis mode are provided in Fig. 7C. We tested the PCECs at 400°C and a current density of 0.6 A cm^{-2} for >2000 hours, achieving negligible degradation in the applied voltage, Faradaic efficiency, and energy efficiency. To the best of our knowledge, these results have validated the feasibility of durable H_2 production in PCECs at 400°C, which greatly reduces the operating temperature and exceeds previous PCEC performance. The stable terminal voltage and Faradaic efficiency suggest no evidence of degradation. Specifically, as shown in figs. S51 and S52, no cracking is observed in the electrolyte, which is essential for high Faradaic efficiency. The durable operation also implies that the positive electrode decomposition or electrolyte-positive electrode delamination is not expected, highlighting the robustness of the redesigned PCECs for H_2 production.

Although there have been several intriguing demonstrations of direct-ammonia PCECs for power generation, their stability was not provided or was poor (*42*–*46*). Decorating negative electrodes with ammonia-cracking catalysts with the aim of improving the catalytic activity still resulted in obvious degradation (*47*, *48*). We recognized that electrolyte ruggedness is essential for PCEC operation on ammonia fuel. Figure 8A displays the OCV of our redesigned direct-ammonia PCECs along with those of previous PCECs, which shows that the OCV of the redesigned PCECs is stable, while the OCV of a previous PCEC gradually decreased and reached <0.6 V after 24 hours. Moreover, both the ASR_O and ASR_P of the redesigned PCECs are stable during prolonged testing. In contrast, the ASR_O of previous PCECs quickly increases (Fig. 8B), which is mainly ascribed to grain boundary fracture (Fig. 8, C and D). Our redesigned PCECs exhibit no cracking after the stability test (Fig. 8, E and F). At a constant current density of 300 mA cm^{-2} at 450°C, the PCEC continuously operates in fuel cell mode on ammonia fuel for 500 hours, with a degradation rate of <0.01 mV/100 hours (Fig. 8G). There are no detectable changes in the PCEC morphology or any cracking or delamination after the long-term stability test (Fig. 8, H and I). Stability testing of various PCECs was conducted at 400° and 500°C on ammonia fuel, further validating the robustness of the redesigned PCECs (figs. S53 and S54).

Figure 8J illustrates the mechanism depicting the impact of electrolyte microstructure and chemical composition on PCEC stability on ammonia fuel. Figure 3 (G and H) shows that a Ba deficiency in the electrolyte promotes the segregation of specific elements (e.g., Yb) along the grain boundary or leads to the formation of impurities on the grain boundary. This, in turn, causes decohesion between contiguous grains. Under aggressive atmospheres, such as ammonia and hydrogen, cracks can initiate and propagate along the grain boundaries, resulting in gas leakage and irreparable degradation as shown in Fig. 8A (figs. S55 and S56).

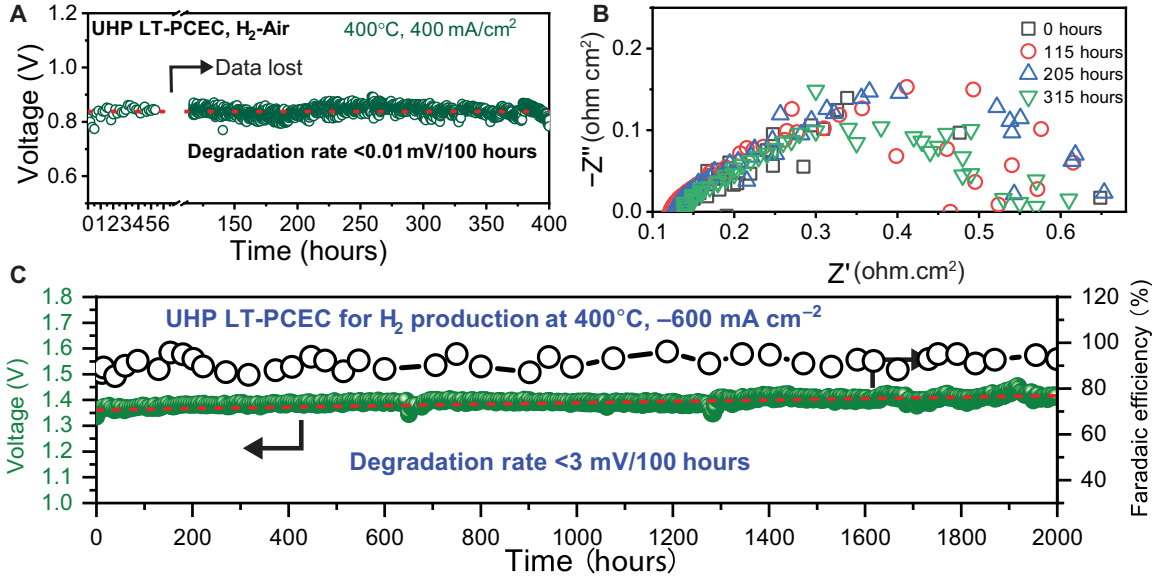


Fig. 7. Stability of redesigned UHP LT-PCECs for power generation in H_2 fuel and H_2 production in steam electrolysis mode. The red dashed lines show the fitted results for determining the degradation rate. (**A**) Long-term stability of a UHP LT-PCEC under H_2-Air at 400°C with an output current density of 400 mA cm^{-2} (cell 26). (**B**) Nyquist plots measured at OCV of the UHP LT-PCEC for long-term stability testing at 400°C (cell 26). (**C**) Long-term stability of a UHP LT-PCEC in electrolysis mode at 400°C with a charging current density of 600 mA cm^{-2} (cell 27).

Downloaded from https://www.science.org at Imperial College London on January 16, 2025

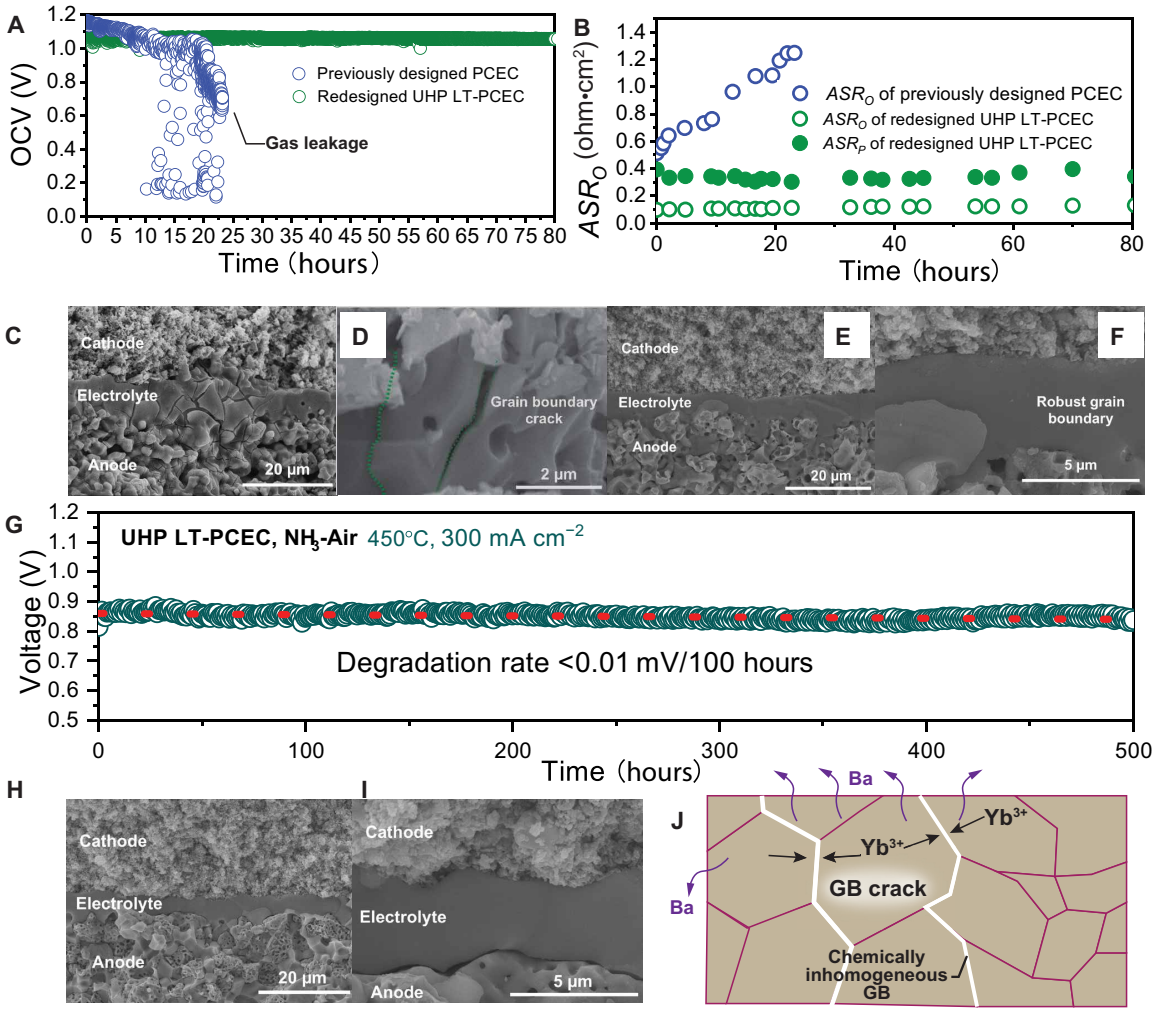


Fig. 8. Stability of redesigned UHP LT-PCECs for power generation in NH_3 fuel. The red dashed lines show the fitted results for determining the degradation rate. (**A**) Comparison of OCV on ammonia fuel for redesigned UHP LT-PCECs (cell 28) and previously designed PCECs (cell 29). (**B**) Comparison of ASR_O and ASR_P on ammonia fuel for redesigned UHP LT-PCECs (cell 28) and previously designed PCECs (cell 29). (**C** and **D**) SEM images of previously designed PCECs (cell 29) after stability testing on ammonia fuel. (**E** and **F**) SEM images of redesigned UHP LT-PCECs (cell 28) after stability testing on ammonia fuel. (**G**) Long-term stability of a UHP LT-PCEC on NH_3-Air at 450°C with an output current density of 300 mA cm^{-2} (cell 30). (**H** and **I**) SEM images of redesigned UHP LT-PCECs (cell 30) after stability testing on ammonia fuel at 450°C. (**J**) Proposed theory of fuel cell stability on ammonia fuel, which shows that the grain boundary chemical homogeneity is important for its robustness and durability.

DISCUSSION

By appropriately pairing the electrolyte with a Ba-rich and fully crystallized negative electrode, a single-grain–thick, chemically homogeneous, robust, and low-resistance electrolyte can be readily fabricated via the conventional cosintering process. Creating the nano-micro positive electrode simultaneously reduces ASR_O and ASR_P while reducing the CTEs and improving the structural stability and electrolyte-positive electrode compatibility. Thus, the UHP LT-PCECs can be redesigned to enhance the fuel cell and steam electrolysis performance and stability at <450°C. The UHP LT-PCECs attain high power densities in fuel cell mode (as high as 1.6 W cm^{-2} at 450°C and 0.2 W cm^{-2} at temperatures as low as 300°C) and exceptional current densities in steam electrolysis mode (over 1.1 A cm^{-2} at 1.4 V and 450°C). Moreover, the PCEC redesign approach can produce chemically homogeneous electrolytes, which mitigates the crack initiation and propagation along the grain boundaries, achieving high and long-term durable fuel cell performance on ammonia fuel and remarkable durability in steam electrolysis mode. These reproducible results further emphasize that through the PCEC materials and architecture design developments presented here, PCECs can be used for power generation and H_2 production at 300° to 450°C, thereby transforming the architectures of and removing previous operational constraints on ceramic electrochemical cells for scaled operation. PCECs can therefore be considered one part of the growing hydrogen economy while leveraging the existing fossil fuel infrastructure and achieving higher energy efficiency and lower CO_2 emissions.

MATERIALS AND METHODS

PCEC powder synthesis

Preparation of the negative electrode powder via the SSRS method

The BCZYYb7111+NiO (SSRS) negative electrode powder consisting of 40 wt % $BaCe_{0.7}Zr_{0.1}Y_{0.1}Yb_{0.1}O_{3-\delta}$ (BCZYYb7111) + 60 wt % NiO was synthesized via the SSRS method. First, a stoichiometric amount of

Downloaded from https://www.science.org at Imperial College London on January 16, 2025

$BaCO_3$, CeO_2, ZrO_2, Y_2O_3, Yb_2O_3, NiO, and 20 wt % corn starch (The amount of corn starch is based on the total weight of BCZYYb7111 and NiO) were ball milled in ethanol using yttria-stabilized zirconia (YSZ) beads (d = 10 mm) for 48 hours. The ball-milled mixture was then transferred into a beaker on a hot plate and continuously stirred at 120°C for 24 hours. A 40 wt % BCZYYb7111 + 60 wt % NiO SSRS negative electrode function layer powder was synthesized using the same procedure but without adding corn starch. The information of all chemicals used in this work can be found in table S15. The information of synthesized powders and their preparation methods can be found in table S16.

Note that in this work, YSZ beads with a diameter of 10 mm were used for the ball-milling process. All YSZ beads were procured from Inframat Advanced Materials. The ball milling was conducted using a roller at a speed of approximately 300 rpm/min.

Preparation of the negative electrode powder via the SSS method

The BCZYYb7111+NiO (SSS) negative electrode powder was synthesized using the SSS method, with a composition of 40 wt % BCZYYb7111 + 60 wt % NiO. First, BCZYYb7111 powder was synthesized by ball milling a stoichiometric mixture of $BaCO_3$, CeO_2, ZrO_2, Y_2O_3, Yb_2O_3, and 1 wt % NiO (based on the total weight of crystallized BCZYYb7111, serving as the sintering aid for crystallizing the BCZYYb7111 during the sintering process) in ethanol using YSZ beads (d = 10 mm) for 48 hours. The resulting powder was dried at 120°C for 24 hours and then calcined at 1350°C for 5 hours to first crystalize the BCZYYb7111. The resulting powder was then crushed in an electric dry crusher at a speed of 12,500 rpm for 3 min, followed by a ball milling again in ethanol using YSZ beads (d = 10 mm) for 48 hours and drying on a hot plate. Next, BCZYYb7111 (SSS) powder was mixed and ball milled with NiO and corn starch in ethanol using YSZ beads (d = 10 mm) for 48 hours with BCZYYb7111, NiO, and corn starch in a weight ratio of 2:3:1. After drying the resulting powder using the same method, the BCZYYb7111+NiO (SSS) negative electrode powder was obtained. The BCZYYb7111+NiO (SSS) negative electrode function layer powder was synthesized using the same processes but without adding corn starch.

Preparation of $BaCe_{0.4}Zr_{0.4}Y_{0.1}Yb_{0.1}O_{3-\delta}$ (BCZYYb4411) electrolyte powder via the wet-chemistry method

The BCZYYb4411 electrolyte was synthesized using the wet-chemistry method (*49*). Initially, a clear solution was obtained by dissolving a stoichiometric amount of Y_2O_3 and Yb_2O_3 in 20 wt % diluted nitric acid solution with continuous stirring at 100°C, which produced the yttrium nitrate and ytterbium nitrate solution. Then, a mixture of stoichiometric amount of $Ba(NO_3)_2$, $Ce(NO_3)_3$•$6H_2O$, and zirconyl nitrate solution (35 wt % in diluted nitric acid) was added to the above solution. To act as complexing and chelating agents, citric acid (CA) and EDTA were added with a CA:EDTA:total cation molar ratio of 2:2:1. The resulting mixture was stirred for 3 hours at room temperature to ensure complete complexation. The pH was adjusted to ~9 by adding aqueous NH_4OH solution. The solution was heated at 250°C until a gel was formed. The gel was immediately moved to a drying oven at 175°C for 24 hours. The resulting black powder was then calcined under air at 1250°C for 5 hours, producing the BCZYYb4411 electrolyte powder for PCEC electrolyte ink preparation.

Preparation of $BaCo_{0.4}Fe_{0.4}Zr_{0.1}Y_{0.1}O_{3-\delta}$ (BCFZY4411) positive electrode powder via the wet-chemistry method

The BCFZY4411 positive electrode powder was synthesized using a wet-chemistry method with stoichiometric amounts of $Ba(NO_3)_2$, $Co(NO_3)_2$•$6H_2O$, $Fe(NO_3)_3$•$9H_2O$, zirconyl nitrate solution (35 wt % in diluted nitric acid), and Y_2O_3 as precursors. Initially, the calculated amount of Y_2O_3 was dissolved in 20 wt % diluted nitric acid solution to prepare the yttrium nitrate solution. The subsequent steps were similar to those of the $BaCe_{0.4}Zr_{0.4}Y_{0.1}Yb_{0.1}O_{3-\delta}$ (BCZYYb4411) electrolyte powder synthesis process. The resulting black powder was dried at 175°C for 24 hours, followed by calcination at 600°C for 5 hours. The powder was then ball milled in ethanol using YSZ beads (d = 10 mm) for 24 hours and dried at 100°C to obtain the positive electrode powder.

Preparation of nano-micro, nano-nano, and nano positive electrode powder

The nano-micro positive electrode powder is composed of 70 wt % nanosized BCFZY4411 that was synthesized using the wet-chemistry method and 30 wt % microsized BCZYYb4411 that was synthesized using the SSS method with 1 wt % NiO added as a sintering aid during sintering. The resulting mixture was ball milled in ethanol using YSZ beads (d = 10 mm) for 24 hours and then dried at 100°C to obtain the nano-micro positive electrode powder.

The nano-nano positive electrode powder consists of 70 wt % nanosized BCFZY4411 that was synthesized using the wet-chemistry method and 30 wt % nanosized BCZYYb4411 that was synthesized using the same wet-chemistry method. During the synthesis of the nanosized BCZYYb4411, a calculated amount of nickel nitrate was added to achieve the same amount of NiO as the microsized BCZYYb4411. Afterward, the resulting nanosized BCFZY4411 and nanosized BCZYYb4411 powder were mixed, ball milled, and then dried to obtain the nano-nano positive electrode powder. The nano positive electrode powder is the pure BCFZY4411 powder that was prepared using the wet-chemistry method.

Preparation of $Sm_{0.2}Ce_{0.7}Ni_{0.1}Ru_{0.05}O_{2-\delta}$ (SDC-Ni-Ru) steam methane reforming catalyst via the wet-chemistry method

SDC-Ni-Ru was synthesized via the wet-chemistry method using a stochiometric amount of $Ce(NO_3)_3$•$6H_2O$, $Sm(NO_3)_2$•$6H_2O$, $Ce(NO_3)_3$•$6H_2O$, $Ni(NO_3)_2$•$6H_2O$, and Ruthenium(III) nitrosyl nitrate solution ($HN_4O_{10}Ru$) as the precursors. The powders were dried at 175°C for 24 hours, calcined at 600°C for 5 hours, ball milled in ethanol using YSZ beads (d = 10 mm) for 24 hours, and then dried at 100°C to obtain the catalyst that will be applied on PCECs.

Synthesis of hydrogen evolution electrode powder for hydrogen pumping testing

The hydrogen evolution electrode, $Sr_2Fe_{1.4}Ni_{0.075}Mo_{0.5}O_{6-\delta}$ (SFNM), was previously validated in our research (*50*) and synthesized using the abovementioned wet-chemistry method with stoichiometric amounts of$Sr(NO_3)_2$,$Fe(NO_3)_3$·$9H_2O$,$Ni(NO_3)_2$·$6H_2O$,and$(NH_4)_6Mo_7O_{24}$·$4H_2O$ as the precursors. The resulting black powder was dried at 175°C for 24 hours, calcined under air at 600°C for 5 hours, ball milled in ethanol using YSZ beads (d = 10 mm) for 24 hours before being dried at 100°C to obtain the SFNM powder, which was used as the hydrogen evolution electrode.

PCEC ink and device fabrication

Preparation of BCZYYb4411 electrolyte ink

The BCZYYb4411 electrolyte powder was mixed with 1 wt % NiO (based on the mass of BCZYYb4411) as the sintering aid, fish oil, b-98 polyvinyl butyral, di-*n*-butyl phthalate, and ethanol. The mixture was then subjected to ball milling using YSZ beads (d = 10 mm) for 4 days.

Preparation of nano-micro, nano-nano, and nano positive electrode slurries

The slurries for the nano-micro, nano-nano, and nano positive electrode slurries were prepared as follows: 5 g of the corresponding

Downloaded from https://www.science.org at Imperial College London on January 16, 2025

positive electrode powder was mixed with 1 g of dispersant [20 wt % solsperse 28000 (Lubrizol) dissolved in α-terpinol] and 0.5 g of binder [5 wt % V-006 (Heraeus) dissolved in α-terpinol]. The mixture was thoroughly ground using a mortar and pestle to produce the positive electrode slurries.

Preparation of $Sm_{0.2}Ce_{0.7}Ni_{0.1}Ru_{0.05}O_{2-\delta}$ (SDC-Ni-Ru) catalyst slurry for internal steam methane reforming

The as-synthesized SDC-Ni-Ru powder was mixed with 1 g of dispersant [20 wt % solsperse 28000 (Lubrizol) dissolved in α-terpinol] and 0.5 g of binder [5 wt % V-006 (Heraeus) dissolved in α-terpinol] and then thoroughly ground using a mortar and pestle. This resulting catalyst ink was solely applied to the PCECs that operate on methane for power generation.

Preparation of SFNM hydrogen evolution electrode slurry

The as-synthesized SFNM powder was mixed with 1 g of dispersant [20 wt % solsperse 28000 (Lubrizol) dissolved in α-terpinol] and 0.5 g of binder [5 wt % V-006 (Heraeus) dissolved in α-terpinol] and then thoroughly ground using a mortar and pestle. This ink was applied to the PCECs for hydrogen pumping experiments, with the goal of determining potential electronic and gas leakage.

Fabricating PCECs with the BCZYYb4411 electrolyte-BCZYYb7111+NiO (SSRS) negative electrode pair

The BCZYYb7111+NiO (SSRS) negative electrode support layer and function layer were fabricated simultaneously using the co-tape casting method. To prepare the negative electrode support layer slurry, BCZYYb7111+NiO (SSRS) negative electrode support layer powder was mixed with menhaden fish oil, b-98 polyvinyl butyral, polyethylene glycol 400, cyclohexanone, di-*n*-butyl phthalate, xylenes, and ethanol. The negative electrode slurry was then ball milled for 24 hours using YSZ beads ($d = 10$ mm). The same procedure was followed to prepare the BCZYYb7111+NiO (SSRS) negative electrode function layer slurry. The function layer was coated first on the Mylar film (with the thickness of ~50 um), followed by the anode support layer (with the thickness of 1.3 mm). Both layers were dried at room temperature for 24 hours and pre-sintered at 800°C for 30 min to remove all organic compounds. Next, the BCZYYb4411 electrolyte ink was spray coated on the top of the anode functional layer and sintered at 1450°C for 5 hours in air. The positive electrode slurry was then applied to the electrolyte using a brush and sintered at 900°C for 5 hours. The effective area of all PCECs used in this work is 0.5 cm^2.

Fabricating PCECs with the BCZYYb4411 electrolyte-BCZYYb7111+NiO (SSS) negative electrode pair

The BCZYYb7111+NiO (SSS) negative electrode support layer and function layer were also fabricated simultaneously using the co-tape casting method, and the slurry preparation and tape casting process were identical to the processes previously mentioned. The same BCZYYb4411 electrolyte ink was spray coated on the BCZYYb7111+NiO (SSS) negative electrode function layer, followed by sintering at 1450°C for 5 hours in air. Three different positive electrode slurries, including nano-micro, nano-nano, and nano positive electrode, were then brush painted on the electrolyte side and sintered at 900°C for 5 hours. The effective positive electrode area of all PCECs used in this study is 0.5 cm^2.

Methane-fueled PCEC single-cell fabrication for power generation

The PCECs with the BCZYYb4411 electrolyte-BCZYYb7111+NiO (SSS) negative electrode pair were used as the half cells. The nano-micro ink was then brush painted on the electrolyte side and sintered at 900°C for 5 hours. The effective positive electrode area is 0.5 cm^2. Then, SDC-Ni-Ru ink was brush painted on the BCZYYb7111+NiO (SSS) negative electrode and dried at 220°C for 30 min. This catalytic layer can enhance the steam methane reforming catalytic activity of PCECs.

PCEC single-cell fabrication for hydrogen pumping testing

The PCECs with the BCZYYb4411 electrolyte-BCZYYb7111+NiO (SSS) negative electrode pair were used as the half cells in this study. The SFNM hydrogen evolution electrode slurry was then brush painted on the electrolyte side and sintered at 1000°C for 5 hours. In this work, the effective electrode area is 0.5 cm^2.

BCZYYb4411 electrolyte pellet preparation for determining the impact of negative electrodes on electrolyte densification and grain growth

The as-synthesized nanosized BCZYYb4411 (with 1 wt % NiO) electrolyte powder was dry-pressed using a carbonized stainless steel die set under a pressure of 150 bar for 2 min, resulting in green pellets of 20-mm diameter and 1-mm thickness. These pellets were placed on different setters, including BCZYYb7111+NiO (SSS) negative electrode setters, BCZYYb7111+NiO (SSRS) negative electrode setters, and alumina setters, and then sintered at 1450°C for 5 hours. The sintered pellets were analyzed via SEM and EDS to investigate the impacts of negative electrode substrates on the electrolyte densification and grain growth.

Structural characterizations

X-ray diffraction

The crystal structures were analyzed using x-ray diffraction (Rigaku MiniFlex II diffractometer with a Cu Kα radiation source operated at 30 kV and 15 mA. The scan speed was 1°/min).

Scanning electron microscope

The microstructure of PCECs and EDS were examined by using the SEMs (Hitachi/S-3400 N and FEI Nova NanoSEM450). For characterizing the PCEC after 2000 hours testing. SEM and EDS analyses were conducted using a Zeiss Auriga Cross Beam system equipped with an INCA X-act EDS detector (Oxford Instruments Ltd., UK). Secondary electron images were acquired at an accelerating voltage of 10 kV with a 30-μm aperture. SEM-EDS mapping and elemental analysis were performed at an accelerating voltage of 20 kV, using the same 30-μm aperture.

SEM-FIB

The microstructure and EDS of PCECs equipped with three different positive electrodes was characterized using the TESCAN S8252G RAMAN-SEM/focused ion beam (FIB). Ga+ FIB was applied to mill the samples.

TEM

The TEM samples were prepared using the FEI HELIOS NANOLAB 600I FIB/SEM. TEM and EDS were performed with an FEI Talos F200X TEM/STEM using a 200-keV accelerating voltage.

Dilatometry

The dilatometry experiments were conducted using the Netzsch DIL 402 Expedis to measure the linear thermal expansion profiles of the positive electrode and electrolyte samples. All samples used in the dilatometry experiments were cylindrical in shape. The positive electrode and electrolyte samples (~0.6 g for each sample) were prepared by using a carbonized stainless steel die set under a pressure of 150 bar for 2 min, resulting in green cylinders. These cylinders were then sintered at 900°C for 5 hours, with the goal of obtaining the same microstructure with the positive electrode layer. The electrolyte cylinder

Downloaded from https://www.science.org at Imperial College London on January 16, 2025

was sintered at 1450°C to achieve a densified sample. The liner thermal expansion profiles of these samples were collected with a heating and cooling rate of 10°C/min. The dilatometer was calibrated and corrected for each measurement. The dimensions of positive electrode and electrolyte samples after final sintering are as follows: Nano positive electrode: ϕ 5.38 mm by 8.60 mm; nano-nano positive electrode: ϕ 5.82 mm by 8.87 mm; nano-micro positive electrode: ϕ 5.88 mm by 8.31 mm; electrolyte: ϕ 5.01 mm by 6.67 mm.

Peeling strength testing

The peeling strength of the positive electrode was evaluated in accordance to the ASTM D903 standard for 180° peeling strength testing (fig. S57). PCECs full cells with three types of positive electrodes were fabricated under identical conditions, and both positive and negative electrodes were clean and dry. The specimens were mounted in the test apparatus by securing the negative electrode using heavy-duty double-sided tape. A rectangular strip of tape was placed on the negative electrode. One end of the tape was affixed to the positive electrode, and the other end was clamped to the test machine and pulled back in a "U" shape. A rectangular strip of tape with a length of 3 cm and a width of 2.5 cm was placed on the negative electrode. One end of the tape was affixed to the positive electrode, and the other end was clamped to the test machine and pulled back in a U shape. All peeling tests were conducted at the same speed, and the peel force was measured in newton. In addition, we selected heavy-duty tape to ensure the accurate separation of the positive electrode from the electrolyte, aiming to represent the interface separation. To address reproducibility, we conducted a total of 15 tests (5 tests for each sample; fig. S37), providing a robust dataset to ensure the reliability of our results.

Electrochemical measurement

PCEC single cell testing in both fuel cell and steam electrolysis modes

Current collection and cell testing stations. The current collectors for both electrodes of PCECs were prepared by painting gold paste onto them. A silver grid was then applied on top of the gold paste to weld the silver wire on both electrodes. The PCECs were sealed onto an alumina tube using a glass sealant (MO ·SCI: 1745P/-45). The negative electrode (anode in fuel-cell mode and cathode in steam electrolysis mode) was exposed to a relatively small alumina tube with a diameter of 16 mm, which controlled the atmosphere around the negative electrode. The positive electrode (cathode in fuel-cell mode and anode in steam electrolysis mode) was exposed to a large quartz tube with a diameter of 50 mm, which controlled the atmosphere around the positive electrode.

Before electrochemical measurements, the negative electrodes of all PCEC cells were first reduced under H_2 [20 standard cubic centimeter per minute (SCCM)] at 600°C for 30 min, upon sealing onto the alumina tube. At each temperature, the cells were kept at a constant temperature for around 15 min to reach an equilibrium state before the electrochemical measurement. The cooling rate was set to be approximately 3.5°C/min. All electrochemical measurements were conducted using the Gamry Reference 3000, Gamry Interface 5000, and Princeton applied research potentiostat at an operating temperature ranging from 600° to 300°C.

PCEC fuel cell testing on hydrogen. The hydrogen with a flow rate of 80 SCCM was fed to the negative electrode. The air or pure oxygen stream with a flow rate of 500 SCCM was fed to the positive electrode.

PCEC fuel cell testing on ammonia. The fuel used in the experiment was ammonia, while air was used as the oxidant. The ammonia flow rate was adjusted on the basis of operating temperature to maximize the fuel utilization. At 600°C, the flow rate was 40 SCCM, while at 550°C, it was 30 SCCM. The flow rate was further reduced to 25 SCCM at 500°C, 20 SCCM at 450°C, and 10 SCCM at 400°C. At the lowest operating temperature of 350°C, the flow rate was 5 SCCM. The air flow rate was maintained constant at 500 SCCM for all temperatures.

PCEC fuel cell testing on methane. The methane to steam ratio was 1:2. The steam concentration was controlled by bubbling CH_4 gas through a customized temperature-controlled bubbler. The CH_4 flow rate was adjusted at different operating temperatures to maximize the fuel utilization, with a flow rate of 16 SCCM at 500°C, 12 SCCM at 450°C, and 8 SCCM at 400°C. The air flow rate remained constant at 500 SCCM for all temperatures.

PCEC steam electrolysis mode testing. The positive electrode was supplied with a mixture of steam and nitrogen, with a steam concentration of 40%, regulated by passing nitrogen gas through a temperature-controlled bubbler. The nitrogen gas flow rate was 100 SCCM. The negative electrode was fed with a pure hydrogen gas stream at a flow rate of 15 SCCM. To enable accurate measurement of hydrogen production rate using gas chromatography (Agilent 3000A), the negative electrode outlet gas was mixed with a nitrogen gas stream to dilute the produced hydrogen. The Faradaic efficiency (*FE* %) was calculated using the following equation

$$FE\,(\%) = \frac{n_{H_2,measured}}{n_{H_2,theoretical}} = \frac{n_{H_2,measured} \times (\mathrm{n} \times F)}{I} \times 100$$

where *FE* (%) is the Faradaic efficiency at a specific current density, $n_{H_2,measured}$ is the measured hydrogen production rate (mol/s), n is 2, *F* is the Faradaic constant (96,485 C mol^{-1}), and *I* is the applied current (A).

PCECs for hydrogen pumping testing. The purpose of this experiment is to confirm that the electrolyte does not exhibit electronic leakage by measuring the Faradaic efficiency during hydrogen pumping testing. During testing, a gas mixture containing 20 vol % H_2 (20 SCCM H_2 + 80 SCCM N_2) was introduced to the positive electrode. The negative electrode was first reduced with 20 vol % H_2 (5 SCCM H_2 + 20 SCCM Ar) for 1 hour, after which it was switched to pure Ar gas with a flow rate of 20 SCCM. An applied current density ranging from 50 to 400 mA/cm^2 was applied for pumping hydrogen. At each current density, the PCEC operated for approximately 30 min to allow the outlet gas concentration reach equilibrium. Figure S58 illustrates the whole hydrogen pumping experiment process. At the positive electrode, the $2H_2 \rightarrow 4H^+ + 4e^-$ electrochemical reaction occurs. This reaction leads to the generation of protons and electrons. The protons are then transported through the electrolyte to the negative electrode. Upon reaching the negative electrode, the protons participate in the reduction process ($4H^+ + 4e^- \rightarrow 2H_2$). This reaction results in the regeneration of molecular hydrogen. To assess the effectiveness of this process, the outlet gas concentration is monitored, and Faradaic efficiency is calculated using an inline gas chromatograph (INFICON 3000 Micro GC).

Supplementary Materials

This PDF file includes:

Supplementary text 1 to 4
Figs. S1 to S58
Tables S1 to S16
References

Downloaded from https://www.science.org at Imperial College London on January 16, 2025

REFERENCES AND NOTES

1. S. Zhai, H. Xie, P. Cui, D. Guan, J. Wang, S. Zhao, B. Chen, Y. Song, Z. Shao, M. Ni, A combined ionic Lewis acid descriptor and machine-learning approach to prediction of efficient oxygen reduction electrodes for ceramic fuel cells. *Nat. Energy* **7**, 866–875 (2022).
2. Z. Wang, Y. Wang, J. Wang, Y. Song, M. J. Robson, A. Seong, M. Yang, Z. Zhang, A. Belotti, J. Liu, G. Kim, J. Lim, Z. Shao, F. Ciucci, Rational design of perovskite ferrites as high-performance proton-conducting fuel cell cathodes. *Nat. Catal.* **5**, 777–787 (2022).
3. D. Clark, H. Malerød-Fjeld, M. Budd, I. Yuste-Tirados, D. Beeaff, S. Aamodt, K. Nguyen, L. Ansaloni, T. Peters, P. K. Vestre, D. K. Pappas, M. I. Valls, S. Remiro-Buenamañana, T. Norby, T. S. Bjørheim, J. M. Serra, C. Kjølseth, Single-step hydrogen production from NH_3, CH_4, and biogas in stacked proton ceramic reactors. *Science* **376**, 390–393 (2022).
4. M. Li, B. Hua, L.-C. Wang, J. D. Sugar, W. Wu, Y. Ding, J. Li, D. Ding, Switching of metal–oxygen hybridization for selective CO_2 electrohydrogenation under mild temperature and pressure. *Nat. Catal.* **4**, 274–283 (2021).
5. S. H. Morejudo, R. Zanón, S. Escolástico, I. Yuste-Tirados, H. Malerød-Fjeld, P. K. Vestre, W. G. Coors, A. Martínez, T. Norby, J. M. Serra, C. Kjølseth, Direct conversion of methane to aromatics in a catalytic co-ionic membrane reactor. *Science* **353**, 563–566 (2016).
6. W. Zhang, X. Hu, Y. Zhou, Z. Luo, G. Nam, Y. Ding, T. Li, Z. Liu, Y. Ahn, N. Kane, W. Wang, J. Hou, D. Spradling, M. Liu, A solid oxide fuel cell runs on hydrocarbon fuels with exceptional durability and power output. *Adv. Energy Mater.* **12**, 2202928 (2022).
7. F. Liu, D. Ding, C. Duan, Protonic ceramic electrochemical cells for synthesizing sustainable chemicals and fuels. *Adv. Sci.* **10**, 2206478 (2023).
8. F. Liu, H. Deng, H. Ding, P. Kazempoor, B. Liu, C. Duan, Process-intensified protonic ceramic fuel cells for power generation, chemical production, and greenhouse gas mitigation. *Joule* **7**, 1308–1332 (2023).
9. F. Liu, H. Deng, D. Diercks, P. Kumar, M. H. A. Jabbar, C. Gumeci, Y. Furuya, N. Dale, T. Oku, M. Usuda, P. Kazempoor, L. Fang, D. Chen, B. Liu, C. Duan, Lowering the operating temperature of protonic ceramic electrochemical cells to <450 °C. *Nat. Energy* **8**, 1145–1157 (2023).
10. E. D. Wachsman, K. T. Lee, Lowering the temperature of solid oxide fuel cells. *Science* **334**, 935–939 (2011).
11. J. Zhang, S. Ricote, P. V. Hendriksen, Y. Chen, Advanced materials for thin-film solid oxide fuel cells: Recent progress and challenges in boosting the device performance at low temperatures. *Adv. Funct. Mater.* **32**, 2111205 (2022).
12. W. Bian, W. Wu, B. Wang, W. Tang, M. Zhou, C. Jin, H. Ding, W. Fan, Y. Dong, J. Li, D. Ding, Revitalizing interface in protonic ceramic cells by acid etch. *Nature* **604**, 479–485 (2022).
13. C. Duan, J. Tong, M. Shang, S. Nikodemski, M. Sanders, S. Ricote, A. Almansoori, R. O'Hayre, Readily processed protonic ceramic fuel cells with high performance at low temperatures. *Science* **349**, 1321–1326 (2015).
14. M. Choi, J. Paik, D. Kim, D. Woo, J. Lee, S. J. Kim, J. Lee, W. Lee, Exceptionally high performance of protonic ceramic fuel cells with stoichiometric electrolytes. *Energ. Environ. Sci.* **14**, 6476–6483 (2021).
15. K. Bae, D. H. Kim, H. J. Choi, J.-W. Son, J. H. Shim, High-performance protonic ceramic fuel cells with 1 μm thick Y:Ba(Ce, Zr)O_3 electrolytes. *Adv. Energy Mater.* **8**, 1801315 (2018).
16. K. Bae, D. Y. Jang, H. J. Choi, D. Kim, J. Hong, B.-K. Kim, J.-H. Lee, J.-W. Son, J. H. Shim, Demonstrating the potential of yttrium-doped barium zirconate electrolyte for high-performance fuel cells. *Nat. Commun.* **8**, 14553 (2017).
17. J. Cao, Y. Ji, Z. Shao, Perovskites for protonic ceramic fuel cells: A review. *Energ. Environ. Sci.* **15**, 2200–2232 (2022).
18. K. Park, H. Bae, H.-K. Kim, I.-G. Choi, M. Jo, G.-M. Park, M. Asif, A. Bhardwaj, K.-S. Lee, Y.-C. Kim, S.-J. Song, E. D. Wachsman, J.-Y. Park, Understanding the highly electrocatalytic active mixed triple conducting $Na_xCa_{3-x}Co_4O_{9-\delta}$ oxygen electrode materials. *Adv. Energy Mater.* **13**, 2202999 (2023).
19. J. Liu, J. K. Kim, Y. Wang, H. Kim, A. Belotti, B. Koo, Z. Wang, W. Jung, F. Ciucci, Understanding and mitigating A-site surface enrichment in Ba-containing perovskites: A combined computational and experimental study of $BaFeO_3$. *Energ. Environ. Sci.* **15**, 4069–4082 (2022).
20. K. Pei, Y. Zhou, K. Xu, H. Zhang, Y. Ding, B. Zhao, W. Yuan, K. Sasaki, Y. Choi, Y. Chen, M. Liu, Surface restructuring of a perovskite-type air electrode for reversible protonic ceramic electrochemical cells. *Nat. Commun.* **13**, 2207 (2022).
21. S. Choi, C. J. Kucharczyk, Y. Liang, X. Zhang, I. Takeuchi, H.-I. Ji, S. M. Haile, Exceptional power density and stability at intermediate temperatures in protonic ceramic fuel cells. *Nat. Energy* **3**, 202–210 (2018).
22. H. An, H.-W. Lee, B.-K. Kim, J.-W. Son, K. J. Yoon, H. Kim, D. Shin, H.-I. Ji, J.-H. Lee, A5 × 5 cm^2 protonic ceramic fuel cell with a power density of 1.3 W cm^{-2} at 600 °C. *Nat. Energy* **3**, 870–875 (2018).
23. Y. Zhou, E. Liu, Y. Chen, Y. Liu, L. Zhang, W. Zhang, Z. Luo, N. Kane, B. Zhao, L. Soule, Y. Niu, Y. Ding, H. Ding, D. Ding, M. Liu, An active and robust air electrode for reversible protonic ceramic electrochemical cells. *ACS Energy Lett.* **6**, 1511–1520 (2021).
24. L. Yang, S. Wang, K. Blinn, M. Liu, Z. Liu, Z. Cheng, M. Liu, Enhanced sulfur and coking tolerance of a mixed ion conductor for SOFCs: $BaZr_{0.1}Ce_{0.7}Y_{0.2-x}Yb_xO_{3-\delta}$. *Science* **326**, 126–129 (2009).
25. H. An, S. Im, J. Kim, B.-K. Kim, J.-W. Son, K. J. Yoon, H. Kim, S. Yang, H. Kang, J.-H. Lee, H.-I. Ji, An unprecedented vapor-phase sintering activator for highly refractory proton-conducting oxides. *ACS Energy Lett.* **7**, 4036–4044 (2022).
26. J. Tong, D. Clark, M. Hoban, R. O'Hayre, Cost-effective solid-state reactive sintering method for high conductivity proton conducting yttrium-doped barium zirconium ceramics. *Solid State Ion.* **181**, 496–503 (2010).
27. D. R. Clark, H. Zhu, D. R. Diercks, S. Ricote, R. J. Kee, A. Almansoori, B. P. Gorman, R. P. O'Hayre, Probing grain-boundary chemistry and electronic structure in proton-conducting oxides by atom probe tomography. *Nano Lett.* **16**, 6924–6930 (2016).
28. D. R. Clark, *Understanding Proton-Conducting Perovskite Interfaces Using Atom Probe Tomography*. (Colorado School of Mines, 2015).
29. D. R. Diercks, B. P. Gorman, A. Manerbino, G. Coors, Atom probe tomography of yttrium-doped barium–cerium–zirconium oxide with NiO addition. *J. Am. Ceram. Soc.* **97**, 3301–3306 (2014).
30. C. Duan, R. Kee, H. Zhu, N. Sullivan, L. Zhu, L. Bian, D. Jennings, R. O'Hayre, Highly efficient reversible protonic ceramic electrochemical cells for power generation and fuel production. *Nat. Energy* **4**, 230–240 (2019).
31. C. Duan, D. Hook, Y. Chen, J. Tong, R. O'Hayre, Zr and Y co-doped perovskite as a stable, high performance cathode for solid oxide fuel cells operating below 500 °C. *Energ. Environ. Sci.* **10**, 176–182 (2017).
32. H. Ding, W. Wu, C. Jiang, Y. Ding, W. Bian, B. Hu, P. Singh, C. J. Orme, L. Wang, Y. Zhang, D. Ding, Self-sustainable protonic ceramic electrochemical cells using a triple conducting electrode for hydrogen and power production. *Nat. Commun.* **11**, 1907 (2020).
33. E. Vøllestad, R. Strandbakke, M. Tarach, D. Catalán-Martínez, M.-L. Fontaine, D. Beeaff, D. R. Clark, J. M. Serra, T. Norby, Mixed proton and electron conducting double perovskite anodes for stable and efficient tubular proton ceramic electrolysers. *Nat. Mater.* **18**, 752–759 (2019).
34. Y. Song, Y. Chen, W. Wang, C. Zhou, Y. Zhong, G. Yang, W. Zhou, M. Liu, Z. Shao, Self-assembled triple-conducting nanocomposite as a superior protonic ceramic fuel cell cathode. *Joule* **3**, 2842–2853 (2019).
35. Y. Song, J. Liu, Y. Wang, D. Guan, A. Seong, M. Liang, M. J. Robson, X. Xiong, Z. Zhang, G. Kim, Z. Shao, F. Ciucci, Nanocomposites: A new opportunity for developing highly active and durable bifunctional air electrodes for reversible protonic ceramic cells. *Adv. Energy Mater.* **11**, 2101899 (2021).
36. Y. Zhang, B. Chen, D. Guan, M. Xu, R. Ran, M. Ni, W. Zhou, R. O'Hayre, Z. Shao, Thermal-expansion offset for high-performance fuel cell cathodes. *Nature* **591**, 246–251 (2021).
37. M. K. Egbo, A fundamental review on composite materials and some of their applications in biomedical engineering. *J. King Saud Univ. Eng. Sci.* **33**, 557–568 (2021).
38. S. Ahmed, F. R. Jones, A review of particulate reinforcement theories for polymer composites. *J. Mater. Sci.* **25**, 4933–4942 (1990).
39. M. Saqib, I.-G. Choi, H. Bae, K. Park, J.-S. Shin, Y.-D. Kim, J.-I. Lee, M. Jo, Y.-C. Kim, K.-S. Lee, S.-J. Song, E. D. Wachsman, J.-Y. Park, Transition from perovskite to misfit-layered structure materials: A highly oxygen deficient and stable oxygen electrode catalyst. *Energ. Environ. Sci.* **14**, 2472–2484 (2021).
40. Y. Chen, B. deGlee, Y. Tang, Z. Wang, B. Zhao, Y. Wei, L. Zhang, S. Yoo, K. Pei, J. H. Kim, Y. Ding, P. Hu, F. F. Tao, M. Liu, A robust fuel cell operated on nearly dry methane at 500 °C enabled by synergistic thermal catalysis and electrocatalysis. *Nat. Energy* **3**, 1042–1050 (2018).
41. K. Li, L. Jia, X. Wang, J. Pu, B. Chi, J. Li, Enhanced methane steam reforming activity and electrochemical performance of $Ni_{0.9}Fe_{0.1}$-supported solid oxide fuel cells with infiltrated Ni-TiO_2 particles. *Sci. Rep.* **6**, 35981 (2016).
42. L. Zhang, W. Yang, Direct ammonia solid oxide fuel cell based on thin proton-conducting electrolyte. *J. Power Sources* **179**, 92–95 (2008).
43. Y. Lin, R. Ran, Y. Guo, W. Zhou, R. Cai, J. Wang, Z. Shao, Proton-conducting fuel cells operating on hydrogen, ammonia and hydrazine at intermediate temperatures. *Int. J. Hydrogen Energy* **35**, 2637–2642 (2010).
44. Y. Aoki, T. Yamaguchi, S. Kobayashi, D. Kowalski, C. Zhu, H. Habazaki, High-efficiency direct ammonia fuel cells based on $BaZr_{0.1}Ce_{0.7}Y_{0.2}O_{3-\delta}$/Pd oxide-metal junctions. *Glob. Chall.* **2**, 1700088 (2018).
45. K. Miyazaki, H. Muroyama, T. Matsui, K. Eguchi, Impact of the ammonia decomposition reaction over an anode on direct ammonia-fueled protonic ceramic fuel cells. *Sustain. Energy Fuels* **4**, 5238–5246 (2020).
46. J. Yang, A. F. S. Molouk, T. Okanishi, H. Muroyama, T. Matsui, K. Eguchi, Electrochemical and catalytic properties of Ni/$BaCe_{0.75}Y_{0.25}O_{3-\delta}$ anode for direct ammonia-fueled solid oxide fuel cells. *ACS Appl. Mater. Interfaces* **7**, 7406–7412 (2015).
47. H. Zhang, Y. Zhou, K. Pei, Y. Pan, K. Xu, Y. Ding, B. Zhao, K. Sasaki, Y. Choi, Y. Chen, M. Liu, An efficient and durable anode for ammonia protonic ceramic fuel cells. *Energ. Environ. Sci.* **15**, 287–295 (2022).
48. F. He, Q. Gao, Z. Liu, M. Yang, R. Ran, G. Yang, W. Wang, W. Zhou, Z. Shao, A new Pd doped proton conducting perovskite oxide with multiple functionalities for efficient and stable power generation from ammonia at reduced temperatures. *Adv. Energy Mater.* **11**, 2003916 (2021).

Downloaded from https://www.science.org at Imperial College London on January 16, 2025

49. C. Duan, R. J. Kee, H. Zhu, C. Karakaya, Y. Chen, S. Ricote, A. Jarry, E. J. Crumlin, D. Hook, R. Braun, N. P. Sullivan, R. O'Hayre, Highly durable, coking and sulfur tolerant, fuel-flexible protonic ceramic fuel cells. *Nature* **557**, 217–222 (2018).
50. F. Liu, L. Fang, D. Diercks, P. Kazempoor, C. Duan, Rationally designed negative electrode for selective CO_2-to-CO conversion in protonic ceramic electrochemical cells. *Nano Energy* **102**, 107722 (2022).
51. D. Huan, N. Shi, L. Zhang, W. Tan, Y. Xie, W. Wang, C. Xia, R. Peng, Y. Lu, New, efficient, and reliable air electrode material for proton-conducting reversible solid oxide cells. *ACS Appl. Mater. Interfaces* **10**, 1761–1770 (2018).
52. D. Huan, W. Wang, Y. Xie, N. Shi, Y. Wan, C. Xia, R. Peng, Y. Lu, Investigation of real polarization resistance for electrode performance in proton-conducting electrolysis cells. *J. Mater. Chem. A* **6**, 18508–18517 (2018).
53. L. Lei, Z. Tao, X. Wang, J. P. Lemmon, F. Chen, Intermediate-temperature solid oxide electrolysis cells with thin proton-conducting electrolyte and a robust air electrode. *J. Mater. Chem. A* **5**, 22945–22951 (2017).
54. S. Choi, T. C. Davenport, S. M. Haile, Protonic ceramic electrochemical cells for hydrogen production and electricity generation: Exceptional reversibility, stability, and demonstrated faradaic efficiency. *Energ. Environ. Sci.* **12**, 206–215 (2019).
55. K. Leonard, Y. Okuyama, Y. Takamura, Y.-S. Lee, K. Miyazaki, M. E. Ivanova, W. A. Meulenberg, H. Matsumoto, Efficient intermediate-temperature steam electrolysis with Y : $SrZrO_3$–$SrCeO_3$ and Y : $BaZrO_3$–$BaCeO_3$ proton conducting perovskites. *J. Mater. Chem. A* **6**, 19113–19124 (2018).
56. K. Li, L. Jia, X. Wang, J. Pu, B. Chi, L. Jian, Methane on-cell reforming in nickel–iron alloy supported solid oxide fuel cells. *J. Power Sources* **284**, 446–451 (2015).
57. Q. Li, X. Wang, L. Jia, B. Chi, J. Pu, J. Li, High performance and carbon-deposition resistance metal-supported solid oxide fuel cell with a nickel–manganese spinel modified anode. *Mater. Today Energy* **17**, 100473 (2020).
58. A. Hagen, X. Sun, B. R. Sudireddy, Å. H. Persson, Metal supported SOFCs for mobile applications using hydrocarbon fuels. *J. Electrochem. Soc.* **167**, 104510 (2020).
59. Y. Yin, S. Li, C. Xia, G. Meng, Electrochemical performance of IT-SOFCs with a double-layer anode. *J. Power Sources* **167**, 90–93 (2007).
60. J. Zhao, X. Xu, W. Zhou, I. Blakey, S. Liu, Z. Zhu, Proton-conducting La-doped ceria-based internal reforming layer for direct methane solid oxide fuel cells. *ACS Appl. Mater. Interfaces* **9**, 33758–33765 (2017).
61. J. Zhao, X. Xu, W. Zhou, Z. Zhu, An in situ formed MnO–Co composite catalyst layer over Ni–$Ce_{0.8}Sm_{0.2}O_{2-x}$ anodes for direct methane solid oxide fuel cells. *J. Mater. Chem. A* **5**, 6494–6503 (2017).
62. C. Jin, C. Yang, F. Zhao, A. Coffin, F. Chen, Direct-methane solid oxide fuel cells with $Cu_{1.3}Mn_{1.7}O_4$ spinel internal reforming layer. *Electrochem. Commun.* **12**, 1450–1452 (2010).
63. B. Hua, N. Yan, M. Li, Y.-F. Sun, Y.-Q. Zhang, J. Li, T. Etsell, P. Sarkar, J.-L. Luo, Anode-engineered protonic ceramic fuel cell with excellent performance and fuel compatibility. *Adv. Mater.* **28**, 8922–8926 (2016).
64. B. Hua, N. Yan, M. Li, Y.-q. Zhang, Y.-f. Sun, J. Li, T. Etsell, P. Sarkar, K. Chuang, J.-L. Luo, Novel layered solid oxide fuel cells with multiple-twinned $Ni_{0.8}Co_{0.2}$ nanoparticles: The key to thermally independent CO_2 utilization and power-chemical cogeneration. *Energ. Environ. Sci.* **9**, 207–215 (2016).
65. D. Konwar, B. J. Park, P. Basumatary, H. H. Yoon, Enhanced performance of solid oxide fuel cells using $BaZr_{0.2}Ce_{0.7}Y_{0.1}O_{3-\delta}$ thin films. *J. Power Sources* **353**, 254–259 (2017).
66. L. Lei, J. M. Keels, Z. Tao, J. Zhang, F. Chen, Thermodynamic and experimental assessment of proton conducting solid oxide fuel cells with internal methane steam reforming. *Appl. Energy* **224**, 280–288 (2018).
67. Y. Chen, Y. Choi, S. Yoo, Y. Ding, R. Yan, K. Pei, C. Qu, L. Zhang, I. Chang, B. Zhao, Y. Zhang, H. Chen, Y. Chen, C. Yang, B. deGlee, R. Murphy, J. Liu, M. Liu, A highly efficient multi-phase catalyst dramatically enhances the rate of oxygen reduction. *Joule* **2**, 938–949 (2018).
68. Y. Niu, Y. Zhou, W. Zhang, Y. Zhang, C. Evans, Z. Luo, N. Kane, Y. Ding, Y. Chen, X. Guo, W. Lv, M. Liu, Highly active and durable air electrodes for reversible protonic ceramic electrochemical cells enabled by an efficient bifunctional catalyst. *Adv.Energy Mater.* **12**, 2103783 (2022).
69. A. Seong, J. Kim, D. Jeong, S. Sengodan, M. Liu, S. Choi, G. Kim, Electrokinetic proton transport in triple (H^+/O^{2-}/e^-) conducting oxides as a key descriptor for highly efficient protonic ceramic fuel cells. *Adv. Sci.* **8**, e2004099 (2021).
70. J. Kim, S. Sengodan, G. Kwon, D. Ding, J. Shin, M. Liu, G. Kim, Triple-conducting layered perovskites as cathode materials for proton-conducting solid oxide fuel cells. *ChemSusChem* **7**, 2811–2815 (2014).
71. A. Seong, J. Kim, J. Kim, S. Kim, S. Sengodan, J. Shin, G. Kim, Influence of cathode porosity on high performance protonic ceramic fuel cells with $PrBa_{0.5}Sr_{0.5}Co_{1.5}Fe_{0.5}O_{5-\delta}$ cathode. *J. Electrochem. Soc.* **165**, F1098–F1102 (2018).
72. M. Shang, J. Tong, R. O'Hayre, A promising cathode for intermediate temperature protonic ceramic fuel cells: $BaCo_{0.4}Fe_{0.4}Zr_{0.2}O_{3-\delta}$. *RSC Adv.* **3**, 15769–15775 (2013).
73. Y. Chen, S. Yoo, K. Pei, D. Chen, L. Zhang, B. deGlee, R. Murphy, B. Zhao, Y. Zhang, Y. Chen, M. Liu, An in situ formed, dual-phase cathode with a highly active catalyst coating for protonic ceramic fuel cells. *Adv. Funct. Mater.* **28**, 1704907 (2018).

Acknowledgments: The Tescan S8252G Raman-SEM/FIB instrument used in this research was purchased with support from the NSF-MRI program (DMR-1828454). **Funding:** This work received support from Nissan Motor Co. Ltd. A22-0455-001 (C.D.), Department of Energy grant DE-FE0032005 (C.D. and P.Ka.), Department of Energy grant DE-SC0021505 (C.D.), the National Aeronautics and Space Administration grant 80NSSC21C0220 (C.D.), Royal Academy of Engineering Award RCSRF/2021-1243, and National Research Foundation of Korea Sejong Science Fellowship-abroad grant RS-2023-00251367 (A.S.). A.S. would like to acknowledge the support from Basic Science Research Program through the National Research Foundation of Korea (NRF) funded by the Ministry of Education (RS-2023-00251367). **Author contributions:** Conceptualization: C.D. and F.L. Methodology: C.D., F.L., and D.D. Investigation: C.D., F.L., D.D., P.Ku., C.G., Y.F., N.D., T.O., M.U., P.Ka., I.G., L.L., L.F., D.C., Z.W., A.S., M.J., and S.S. Visualization: C.D. and F.L. Funding acquisition: C.D. Project administration: C.D. Supervision: C.D. Writing—original draft: C.D. and F.L. Writing—review and editing: C.D., F.L., D.D., C.G., Y.F., N.D., T.O., M.U., P.Ka., I.G., L.L., F.L., Z.W., A.S., S.S., M.J., and D.C. **Competing interests:** Part of this work is financially supported by the Nissan Motor Co. Ltd. (A22-0455-001). The funder participates in the decision to publish and preparation of the manuscript. Coauthors, including M.J., C.G., Y.F., and N.D., are employed in Nissan Technical Center North America (NTCNA), Farmington Hills, MI, USA. Coauthors, including T.O. and M.U., are employed in Nissan Research Center, Nissan Motor Company Limited, Yokosuka, Kanagawa, Japan. C.D., F.L., L.F., N.D., M.J., C.G., Y.F., T.O., and M.U. are authors on a patent application filed by Kansas State University Research Foundation, Nissan North America Inc., Nissan Motor Co. Ltd. (no. 63/580,917, filed 6 September 2023). The authors declare that they have no other competing interests. **Data and materials availability:** All data needed to evaluate the conclusions in the paper are present in the paper and/or the Supplementary Materials.

Submitted 6 May 2024
Accepted 11 December 2024
Published 10 January 2025
10.1126/sciadv.adq2507

Downloaded from https://www.science.org at Imperial College London on January 16, 2025